2012

Two-Photon Direct Frequency Comb Spectroscopy of Rubidium

Sophia Lee Chen
Oberlin College

Two-Photon Direct Frequency Comb Spectroscopy of Rubidium

Sophia Chen
Dept. of Physics and Astronomy
Oberlin College

Honors Thesis
April 2, 2012

Summary

Spectroscopy is a powerful tool for understanding the fundamental structure of atoms. In this thesis, we explore the use of an optical frequency comb in a technique called multi-photon direct frequency comb spectroscopy (DFCS) to study the spectrum of rubidium. An optical frequency comb is a phase-stabilized, mode-locked laser with ultrashort pulsed output in the time domain and a range of equally spaced modes in the frequency domain. With a frequency-stabilized frequency comb, absolute frequency measurements can be made to high precision.

The uniqueness of this experiment lies in both the simplicity of the setup and the use of velocity selective resonance to eliminate Doppler broadening. This experiment uses a vapor cell, simple and cheap to manufacture, as an atom source. The laser light from the frequency comb is filtered to contain the necessary frequencies for two-photon transitions in rubidium from the ground state, $5S_{\frac{1}{2}}$, to an upper state, either $5D_{\frac{3}{2}}$ or $5D_{\frac{5}{2}}$, through an intermediate state, either $5P_{\frac{1}{2}}$ or $5P_{\frac{3}{2}}$. The beam is aligned to go through a rubidium vapor cell and is then reflected onto itself back into the cell. Some of the atoms undergo the two-photon transition, and the fluorescence from the decay of the excited atoms is measured by a photomultiplier tube interfaced with a computer. This fluorescence, plotted as a function of one of the frequency parameters of the frequency comb, results in a high-resolution spectrum.

The experiment also bypasses the one of the biggest complications of using a vapor cell for spectroscopy. A vapor cell contains atoms that follow a Maxwell-Boltzmann velocity distribution. In spectroscopy, this velocity distribution usually leads to Doppler broadening of the spectral line. However, we largely avoid Doppler broadening by counterpropagating the two beams at the vapor cell. This way, we excite a single velocity class of atoms.

In addition, we ran theoretical calculations of the spectra using Mathematica and compared these spectra to our data to better understand our system. In terms of the positions of the peaks, the calculated spectra had good qualitative agreement with the experimental spectra. However, detailed features of the measured spectra, such as linewidth and relative amplitudes of the spectral peaks, do not agree with calculations. These features are still under investigation.

Direct frequency comb spectroscopy is a relatively new technique. Although the energy levels in rubidium have already been measured to extremely high precision with other methods, this experiment demonstrates how DFCS can be applied. The experimental setup is relatively simple that it could be extended to the spectroscopy of less precisely known atoms or more complicated systems.

This work is dedicated to all the future Stalnaker lab students, especially those of you who will read this thesis and bemoan the lack of clarity. May you fill in the margins of this text with better physics and prettier plots, and I hope your long nights in the Stalnaker lab are filled with fruit chews, granola bars, Altoids, and other relatively nutritious snacks.

Acknowledgments

First, I would like to thank my adviser, Jason Stalnaker, for giving me the opportunity of working in his lab. His patience, enthusiasm, support, and top-notch pedagogical ability have been invaluable in my undergraduate experience and have inspired me to continue my physics studies. Under his guidance, I have learned to appreciate the elegance of atomic physics, the character-building frustration that accompanies scientific research, and the utility of banging on an experiment with a screwdriver.

I'd also like to thank my lab partner, Michael Rowan. Together we have mastered the art of epoxy, cardboard, masking tape, and spray paint. I am also indebted to all the students who have worked in the Stalnaker lab to build the groundwork on which this experiment rests. Particularly, I would like to thank Sean Bernfeld for his work on comb stabilization, and Will Striegl, who worked on the first incarnation of this experiment.

Thanks to the Oberlin Department of Physics and Astronomy for providing me with the resources for an exciting and fruitful undergraduate career.

In addition, I would like to thank my friends for their support. Thanks to other honors students Christopher Pierce and Jacob Baron, for staying up late with me in productivity and procrastination and helping me through problem sets and new physics concepts. (Also, thank you, Jacob, for not changing bits of my thesis when I left myself logged on the computer.) I must also acknowledge my main man, Chloë Dalby. Thank you for the many late-night conversations that propelled me into writing this thesis instead of devolving into a couch potato, and for providing me with nonsensical conversation when I needed a break.

Finally, I am grateful for the support of my family. Thanks for continuing the flow of encouragement even during my frequent bouts of crabbiness during the completion of this thesis.

Contents

List of Figures **vii**

1 Introduction **1**

2 Optical Frequency Combs **5**

2.1 Introduction to Frequency Combs 5

2.2 Lasers 7

2.3 Mode-Locking 8

2.4 Stabilization 14

2.5 Direct Frequency Comb Spectroscopy 19

3 Theoretical Discussion **21**

3.1 Spectroscopic notation 21

3.2 More about rubidium 22

3.3 Fine and hyperfine splitting of energy levels 24

3.3.1 Fine Structure 24

3.3.2 Hyperfine Structure 26

3.3.2.1 Hyperfine Coefficient A_J 27

3.3.2.2 Hyperfine Coefficient B_J 32

3.4 Isotope Shifts 34

3.5 The Character of Spectral Lines 34

3.5.1 Natural Line Width 34

3.5.2 Doppler Broadening 36

3.5.3 Other Types of Broadening 36

3.6 Transition Probabilities 38

3.6.1 Clebsch-Gordan Coefficients 39

3.6.2 Wigner-Eckart Theorem 40
3.6.3 Relative Transition Probabilities 41
3.7 Velocity Selective Resonance 44

4 Experiment **47**
4.1 Setup 47
4.2 Resonance from Counterpropagating and Copropagating Beams 51
4.3 Controlling Systematic Uncertainty 52

5 Results **53**
5.1 Spectra Calculations 53
5.2 Data Averaging 54
5.3 Peak Identification and Analysis 54
5.4 Sources of Uncertainty 60
5.4.1 Frequency Standard Characterization 60
5.5 Conclusions and Future Work 64

A Mathematica Spectra Calculations **67**

Appendices **67**

References **77**

List of Figures

1.1 Frequency-domain output of an optical frequency comb 2

2.1 Pulsed laser vs. cw laser in the time domain 6
2.2 Output spectrum of our comb 6
2.3 Interaction of light and matter 8
2.4 The modes of a planar cavity 9
2.5 The bow-tie cavity of our comb 9
2.6 Carrier and carrier envelope functions 11
2.7 Phase shift in the carrier function 11
2.8 Dispersive pulse 12
2.9 Chirped mirrors 13
2.10 Hard-aperture Kerr lensing 13
2.11 Stabilization of f_{rep} block diagram 15
2.12 Stabilization of f_0 block diagram 17
2.13 Frequency division used for phase-locking 18

3.1 Energy levels of interest in rubidium 23
3.2 Hyperfine energy levels of rubidium 25
3.3 Angular momentum addition 26
3.4 Semiclassical model of magnetic dipole moment 27
3.5 Example of hyperfine energy splitting 31
3.6 Definitions for multipole magnetic moment expansion for finding B_J . . 33
3.7 Doppler effect 36
3.8 An example of a three-level system in rubidium 42
3.9 Counterpropagating beams 45

LIST OF FIGURES

4.1 Setup of rubidium DFCS experiment 48
4.2 Transmission spectra of interference filters 49
4.3 Rubidium vapor density as a function of temperature 50
4.4 Transimpedance amplifier 50
4.5 Counterpropagating beams 51

5.1 Measured spectrum with 770 nm filter 55
5.2 Measured spectrum with 780 nm filter 56
5.3 Measured spectrum with 785 nm filter 57
5.4 Measured spectrum with broad range red filter 58
5.5 Measured spectrum with different polarizations 59
5.6 Allan deviation of rubidium frequency standard 61
5.7 Allan deviation of clock compared to Allan deviation of f_{rep} lock 63

1

Introduction

The discovery of new physics has been contingent on the precision of experimental measurements. For example, precision spectroscopy experiments have resulted in the observation of fine and hyperfine structure, the Zeeman and Stark effects, and more, helping us confirm and develop new theories about atomic structure and gain deeper insight into fundamental physics.

In addition to probing the mysteries of the universe, these precision measurements also have practical applications. For example, precision measurements have been central to the definition of our fundamental units. Every experiment is limited by the uncertainty in its units. Thanks to precision spectroscopy, the second is now the most precisely realized fundamental unit, defined as 9,192,631,770 periods of oscillation in the radiation between the two hyperfine transitions of the ground state of cesium-133 [1]. The measurement of this transition was a direct result of precision microwave spectroscopy. The most precise clocks today, atomic clocks, are referenced to atomic transitions. Atomic clocks are now used in a variety of applications, including GPS satellites. Some other fundamental units, such as the meter, which is defined by the speed of light, have now been defined in terms of the second so that distance measurements can reap the same degree of precision as time measurements [2].

In this experiment, we explore a relatively new high-precision spectroscopic technique, two-photon direct frequency comb spectroscopy (DFCS), to study the spectrum of rubidium. While experiments with atomic rubidium are useful in terms of theory comparisons, and rubidium also has applications to atomic clocks and precision magnetometry (see Section 3.2), rubidium has already been studied to very high precision

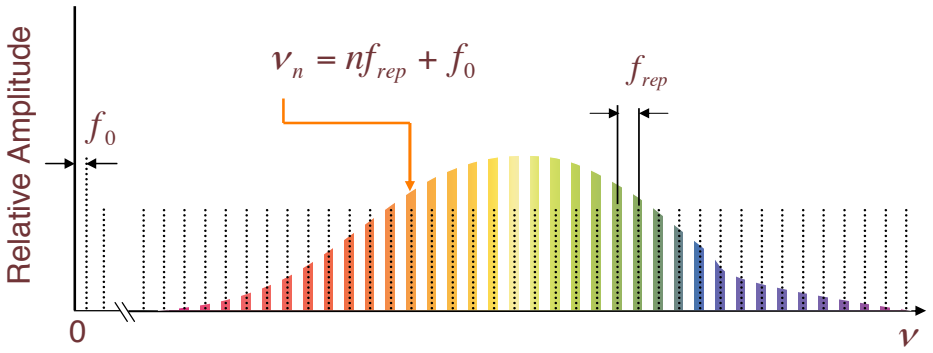

Figure 1.1: The frequency-domain output of an optical frequency comb. Direct frequency comb spectroscopy uses the output of the comb for spectroscopy. The labeled parameters include f_0, the offset frequency from zero, and f_{rep}, the frequency spacing between the modes, known as the repetition rate. Each mode is defined by the relation $\nu_n = nf_{rep} + f_0$, where n is the mode number. See Chapter 2 for more details.

– for example, see Refs. [3, 4, 5]. Thus, in the case of this experiment, our motivation is to study the technique rather than the system. Consequently, in our analysis, we have not made precision frequency measurements.

The technique involves the use of the direct output of a femtosecond optical frequency comb for spectroscopy. An optical frequency comb is a mode-locked, phase-stabilized laser. The time-domain output of the frequency comb is a series of pulses on the order of tens of femtoseconds (10^{-14}), separated by times on the order of nanoseconds. In the frequency domain, pictured in Figure 1.1, the comb consists of hundreds of thousands of modes, equally spaced in frequency. These modes look like the teeth of a comb, hence the name. We go into more detail about frequency combs in Chapter 2.

We use a rubidium vapor cell, which is a glass cell filled with a sample of rubidium. The advantage of a vapor cell is its simplicity and low cost to manufacture–they can be purchased for a couple hundred dollars. The vapor cell is heated such that some of the rubidium is vaporized, and the atoms in the vapor are used for spectroscopy.

However, vapor cells usually complicate precision spectroscopy because of the velocity distribution of the atoms, which follow Maxwell-Boltzmann statistics. Due to the Doppler effect, in the lab frame, different velocities of atoms observe the same frequency of light to be different frequencies. Thus, instead of having a narrow resonance peak, the spectrum is smeared out because the atoms have a large distribution of resonant frequencies. This smearing is known as *Doppler broadening* and makes precision

frequency measurement difficult.

However, we bypass Doppler broadening by using counterpropagating beams – that is, beams that have antiparallel wave vectors – in a two-photon transition. We select a range of frequencies of the frequency comb using an interference filter and use it to excite rubidium in a vapor cell to an intermediate state. Then, because the transitions of interest are very close in frequency, we are able to reflect that same beam of light back through the vapor cell, and we look for the transitions where first beam excites the atoms to an intermediate state and the reflected beam excites the atoms to a final state. The first beam and its reflected beam makes it such that only atoms of a single velocity class are excited, which leads to a theoretically Doppler-free peak. This technique, which we call *velocity selective resonance*, is explained in more detail in Section 3.7. We detect the fluorescence from the decay of the atoms that have undergone the two-photon transition, and by plotting the fluorescence as a function of one of the frequency parameters of the comb, we generate a spectrum.

In addition, the interaction of atoms and very short, high-intensity pulses is a relatively new area of study. We hope that in our further analysis of this technique to learn more about how atoms interact with resonant ultra-short, phase-coherent pulses.

In parallel with the experimental measurement, we also ran spectral calculations and included all the theoretical parameters we considered in the calculation. These spectra calculations were then compared with the experimentally measured spectra. Analysis of these spectra is ongoing, and discrepancies between the theoretically calculated spectra and our experimentally measured spectra are an area of future interest.

This experiment was conducted both for the exploration of the interaction of atoms with resonant ultra-short, phase-coherent pulses, and also for the study of a new and simple spectroscopic technique.

2

Optical Frequency Combs

2.1 Introduction to Frequency Combs

A frequency comb is the output of a phase-stabilized, mode-locked laser, with applications ranging from optical metrology, optical clocks, and, in the case of this experiment, atomic spectroscopy.

Frequency combs can be understood in the time domain or the frequency domain. In the time domain, the frequency comb is a sequence of high-intensity phase-coherent pulses on the order of tens of femtoseconds (10^{-14} seconds) long. The pulses are spaced on the order of nanoseconds apart. The frequency-domain picture is the Fourier transform of the pulse and consists of hundreds of thousands of discrete frequencies called modes, spaced equally in frequency by the inverse of the time between pulses, seen in Figure 1.1. This picture can be contrasted with the familiar continuous wave (cw) monochromatic laser, which consists of one frequency in the frequency domain and a continuous amplitude in the time domain. A comparison of the time domain pictures of the pulsed and cw lasers are shown in Figure 2.1. The particular frequency spectrum of our comb taken with an optical spectrum analyzer is pictured in Figure 2.2. Note that the teeth of the comb cannot actually be resolved by the spectrum analyzer, as a 20 nm passband has on the order of $\sim 10,000$ modes.

Each comb mode can be described using the comb equation

$$\nu = f_0 + n f_{rep}, \tag{2.1}$$

where f_0 is an offset frequency from zero, n is the mode number, and f_{rep} is the inverse

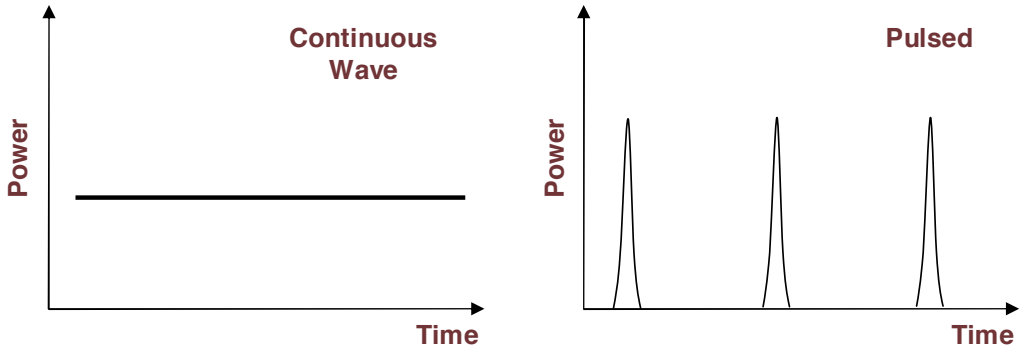

Figure 2.1: The time-domain output of a cw laser and a pulsed laser. Figure from Ref. [6].

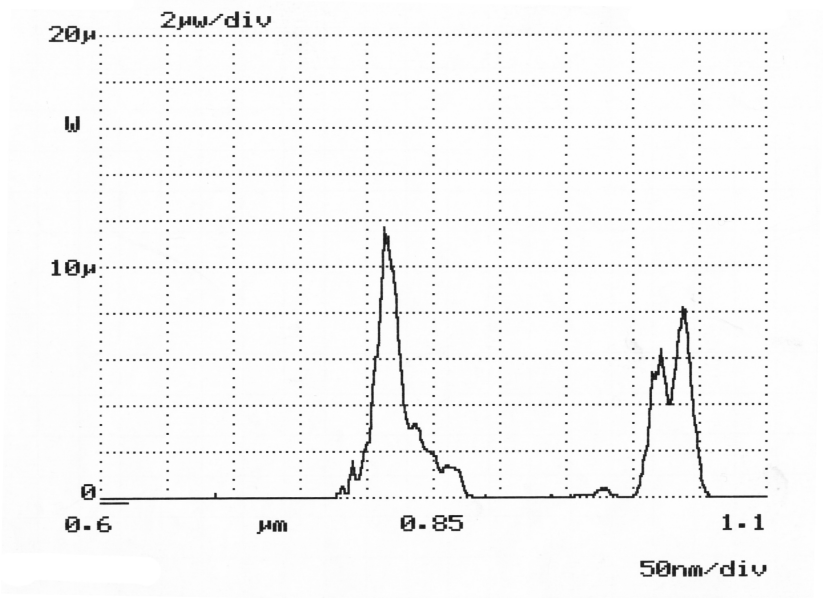

Figure 2.2: This spectrum shows the frequency output of our comb using an optical spectrum analyzer, with wavelength on the horizontal axis and power on the vertical axis. The power of the spectrum peaks around 800 nm and 1050 nm. The teeth of the comb depicted qualitatively in Figure 1.1 are too narrow to resolve with this spectrum analyzer; a 20 nm passband in the optical range corresponds to ∼10,000 modes.

of the inter-pulse period. The parameters f_0 and f_{rep} are described in more detail in Section 2.3.

The optical frequency comb is a bridge between optical and microwave frequencies, which is important because modern electronics are not fast enough to count optical frequencies (∼THz), but they can count microwave frequencies (∼GHz) very precisely. While the frequencies of the comb are in the optical range, f_{rep} and f_0 are in the microwave. By stabilizing f_0 and f_{rep}, all of the modes of the frequency comb are stabilized. Thus, the frequency comb allows optical experiments to be performed to the same level of precision as microwave frequency measurements [7].

The emergence of the femtosecond frequency comb in the 1990's has greatly simplified precision spectroscopy and optical frequency metrology by allowing different experiments to be performed with one laser. In this experiment, we explore the use of the frequency comb as a spectroscopic tool for two-photon transitions in rubidium. As we shall see in Chapter 4, because of the comb's versatility, the setup for rubidium could easily be modified for spectroscopy of a different atom.

The following sections briefly explore the theory behind lasers, mode-locking, the frequency stabilization of our comb, and the technique used in this experiment, direct frequency comb spectroscopy.

2.2 Lasers

Matter can interact with light in three ways: through absorption, spontaneous emission, and stimulated emission, shown in Figure 2.3. Lasers (Light Amplification by Stimulated Emission of Radiation) operate via stimulated emission–where an excited atom, instead of transitioning to a lower state by spontaneous emission, interacts with a photon with the same energy as the spacing between the upper state and the lower state. This causes the atom to emit a photon with the same frequency, phase, and direction as the incident photon.

A laser has three requirements to function: a gain medium, a pump to create population inversion within the gain medium, and an optical resonator. The purpose of the gain medium is straightforward; it produces the photons involved in lasing. For example, in the He-Ne laser, the neon atoms are the gain medium.

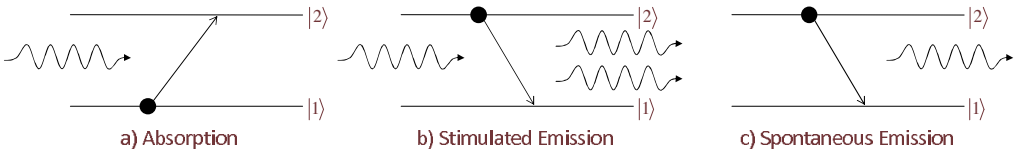

Figure 2.3: The three ways light interacts with matter in a two-level system. Figure (a) shows a particle absorbing a photon to go into the upper state; figure (b) shows an incoming photon stimulating a particle in the upper state to emit two additional photons of the same frequency and phase; figure (c) shows a particle in the upper state emitting a photon with the same energy as the spacing of the two levels. Figure from Ref. [6].

A pump must provide the energy to create population inversion, which is necessary for lasing. Population inversion occurs when more atoms are in the upper state than in the lower state. Such a state is necessary because rates of stimulated emission and stimulated absorption are dependent on the difference of the population of the excited state and the population of the deexcited state. Without pumping, the population of the excited state would be less than the population of the deexcited state, and an atom would be more likely to absorb an incident photon than to undergo stimulated emission, which means lasing would not occur.

Once a population inversion is created, an optical resonator amplifies the stimulated emission. In this experiment, the optical resonator is a set of mirrors that send the light back through the gain medium, leading to the emission of more stimulated photons, creating a usable laser.

A more detailed explanation of lasers can be found in Ref. [8].

2.3 Mode-Locking

A laser cavity can support many different frequencies of light; these frequencies are called the modes of the cavity. The laser used in this experiment uses a titanium-doped sapphire crystal (Ti:sapphire) as its gain medium. Because energy levels are not discrete frequencies, a specific transition can emit a range of frequencies. This range is called the transition's *gain bandwidth*. Ti:sapphire lasers are the most popular source of femtosecond pulses because they have the largest gain bandwidth, which means that a Ti-sapphire laser cavity can support many more modes than most other materials.

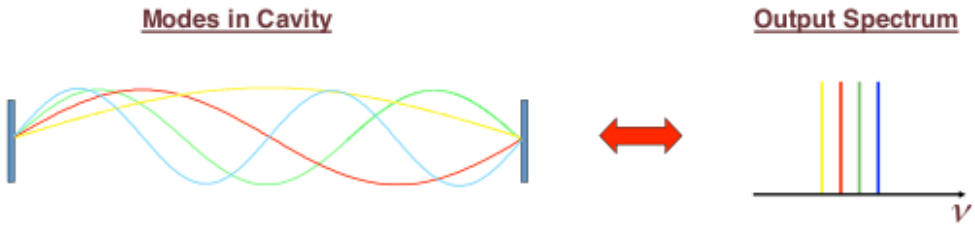

Figure 2.4: The first four modes of a planar cavity are standing waves of the cavity. The spatial-domain picture is shown on the left, and the frequency-domain picture is on the right.

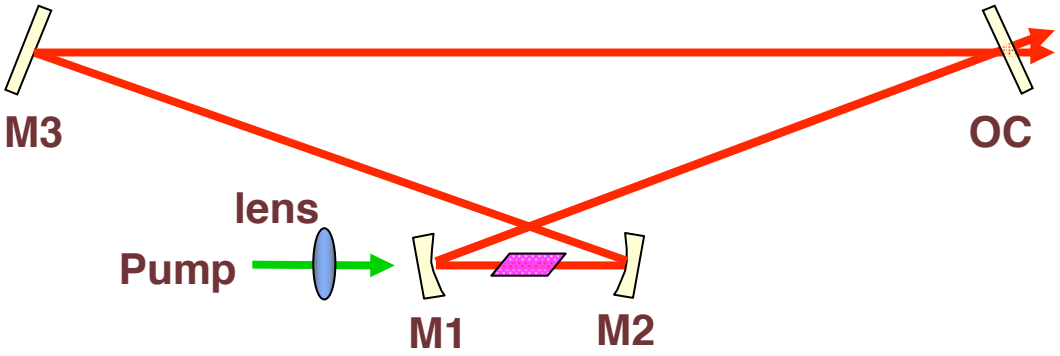

Figure 2.5: Instead of a planar cavity, our laser has a bow-tie cavity. With every round-trip around the cavity, some of the light escapes the cavity through a partially transparent mirror called the output coupler, labeled OC here. This light forms the pulse. The other mirrors are labeled M1, M2, and M3.

The more modes that are phase-locked together, the shorter the pulse is in the time domain.

These modes occur in three dimensions: if we consider a laser cavity of length L in the z direction, the modes along z are called *longitudinal*, and the modes along x and y are called *transverse*. Although our laser cavity is bow-tie shaped, pictured in Figure 2.5, here we will gain a qualitative understanding of mode-locking by considering a planar laser cavity where only longitudinal modes are allowed. For a non-dispersive cavity, i.e. one that has an index of refraction independent of wavelength, the modes have a half-wavelength that is an integer multiple of the length of the cavity. For example, given a nondispersive planar cavity of length L, the wavelengths λ of the modes are given by $m\frac{\lambda}{2} = L$, where m is an integer, pictured in Figure 2.4. The modes are equally separated in frequency by $\Delta\nu = \frac{c}{2L}$.

Mode-locking refers to introducing a fixed-phase relationship among the different modes, such that the different modes interfere to form a pulse. This fixed-phase relationship is called phase coherence. In a laser that is not mode-locked, the different modes of the cavity oscillate independently, and the time-domain transformation of each frequency spectrum does not form a pulse. When all the frequencies of the comb are forced to have a fixed phase relationship, they add constructively to form a pulse. In the time domain, this can be pictured as all the modes of different frequencies adding constructively at one point, resulting in an intense and short pulse of light. The average intensity is the same as that of a cw laser, which means that the pulse has very high peak intensity.

The time dependence of the resultant pulse can be described by two functions, pictured in Figure 2.6. One is a rapidly oscillatory function called the carrier, and it is multiplied by a slowly varying function called the carrier-envelope, or envelope function, that determines the amplitude of the pulse. Due to dispersion in the cavity, the velocity of the envelope, or the speed of the peak of the pulse, is different from the phase velocity, which describes the evolution of the phase of each of the frequency components of the pulse. This results in a phase shift of the carrier wave with respect to the envelope function, pictured in Figure 2.7. A constant phase shift $\Delta\phi$ corresponds to a constant shift to the entire frequency spectrum in the Fourier transform. The offset

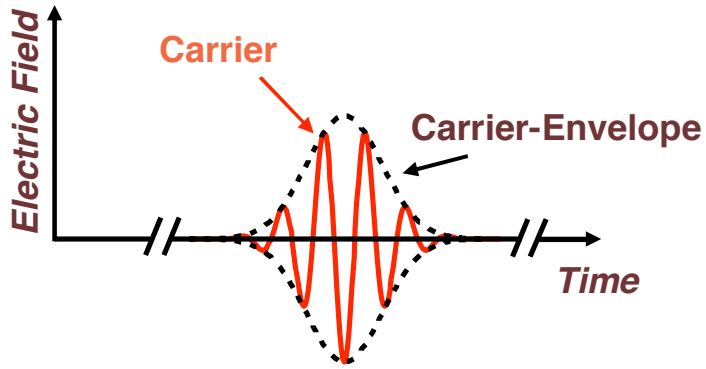

Figure 2.6: The time dependence of the pulses from the comb can be described by two functions, the carrier and the carrier envelope. The carrier is the rapidly oscillating function, and the carrier envelope is the more slowly varying envelope function.

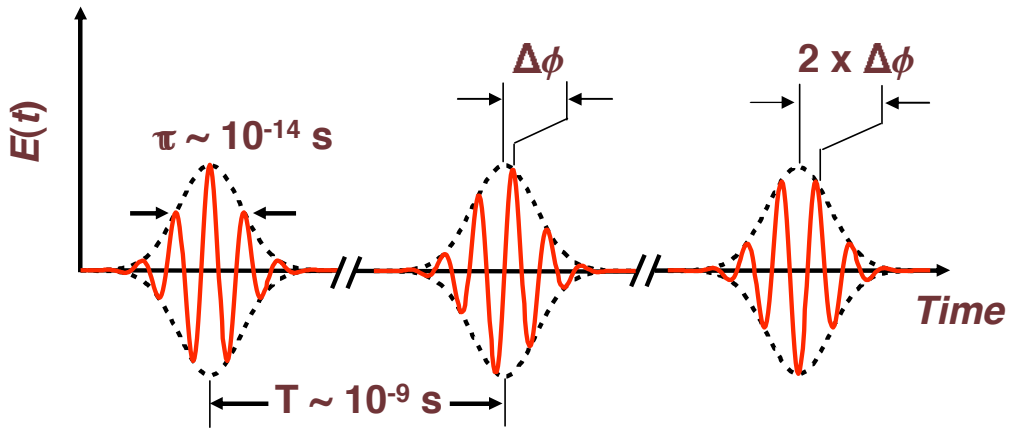

Figure 2.7: Due to dispersion in the laser cavity, the group velocity and the phase velocity of the pulse are different, leading to a phase shift $\Delta\phi$ in the carrier with respect to the group velocity phase. This $\Delta\phi$ is used to define the offset frequency f_0.

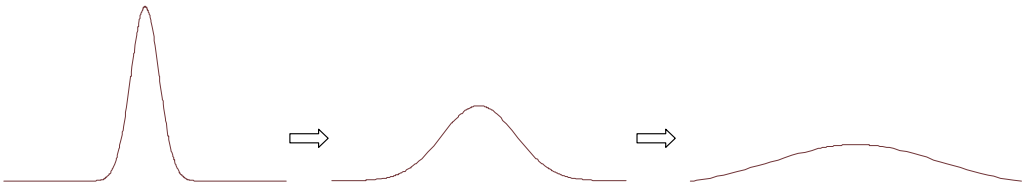

Figure 2.8: In a dispersive cavity, a pulse broadens in time because the group velocity gets more out of phase with each trip around the cavity.

frequency f_0 is defined by this phase shift $\Delta\phi$:

$$f_0 = \frac{\Delta\phi}{2\pi} f_{rep}. \tag{2.2}$$

The repetition rate f_{rep} is defined as the inverse of the inter-pulse period, or

$$f_{rep} = \frac{1}{T}, \tag{2.3}$$

where T is the time it takes for a pulse to travel around a cavity of length L:

$$T = \frac{L}{\bar{v}_g}. \tag{2.4}$$

Here $\bar{v}_g$ is the average velocity of the pulse, which is the average of the group velocities of all its frequency components. This is the speed of the peak of the pulse.

The above description assumes equally spaced modes. But a typical laser cavity is dispersive, which means that its index of refraction is wavelength-dependent. Without mode-locking, each of the modes travels the laser cavity at a different speed. If all the cavity modes are in phase at $t = 0$ and add constructively to form a pulse, after one round trip around the cavity, the modes are still mostly in phase and produce a longer pulse with smaller amplitude, as shown in Figure 2.8. But as these round trips continue, eventually the modes will be all out of phase and will not form a pulse.

This spreading of the pulse in time is compensated by the use of chirped mirrors. Chirped mirrors are designed such that the different wavelengths reflect at different depths on the mirror surface. As the pulse travels through the cavity, it spreads out, but the pulse is then recompressed when it hits the mirrors. The pulse length and bandwidth are primarily determined by the reflectivity and dispersion of the mirrors.

In order to first generate pulses in the cavity, we must cause random fluctuations

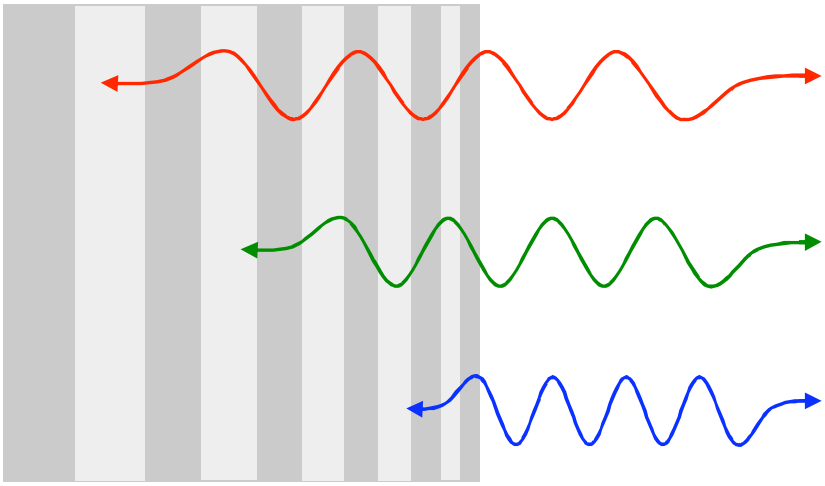

Figure 2.9: Different wavelengths reflect at different wavelengths when they hit chirped mirrors. This compensates for the dispersion effect that causes the spreading out of the pulse in time. Figure taken from Ref. [6].

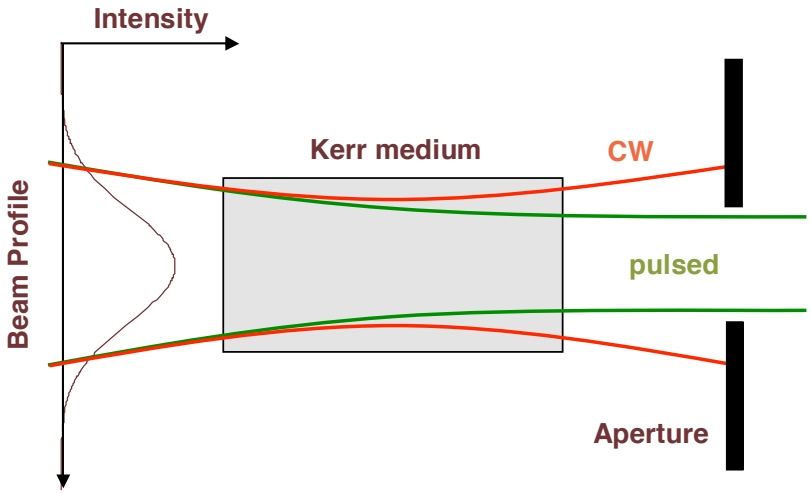

Figure 2.10: Hard-aperture Kerr lensing. Kerr lensing causes the crystal to act as a lens with an index of refraction dependent on intensity. The pulsed beam is much higher in intensity than the cw beam, so it focuses differently. In hard-aperture Kerr lensing, an aperture is used to cut the cw beam off. Figure taken from Ref. [6].

in the phases of the different modes of the cavity. Sometimes these fluctuations will lead to a brief pulse formation that will be stabilized. If this pulse does form, it will be amplified by the Kerr lens effect and result in mode-locking. To cause these random fluctuations, we tap on the curved mirror, pictured as M2 in Figure 2.5, with a screwdriver.

Once a pulse is generated, it is amplified by an effect known as Kerr lensing or self-focusing. The Kerr effect is a third-order, nonlinear interaction ($\chi^{(3)}$) between light and the Ti:sapphire crystal. In particular, it introduces an intensity-dependent term for the index of refraction of the crystal. The average intensity of the laser is the same, regardless if the laser is pulsed or cw. However, if the laser is pulsed, the instantaneous intensity of the pulse is much higher than the instantaneous intensity of the cw beam.

Because the pulses have higher intensity than the cw beam, the pulsed beam has a different index of refraction than the cw beam. Effectively, this means that the crystal acts as lens that focuses the pulsed lens and the cw beam differently.

The Kerr effect can be applied to mode-locking in two ways: with a hard aperture or a soft aperture. In the hard aperture case, pictured in Figure 2.10, the high intensity pulse is focused through an aperture, while the cw beam is cut off [9].

The laser in this experiment uses soft aperture Kerr lensing. The cavity is aligned such that the lensing effect in the Ti:sapphire crystal results in a better overlap with the pump laser, which results in higher gain for the pulses with high peak power.

2.4 Stabilization

As seen in equation (2.1), f_0 and f_{rep} constitute the only two degrees of freedom in each comb mode. In other words, by stabilizing f_0 and f_{rep}, every comb mode has been stabilized. In our setup, f_0 and f_{rep} are independently measured and stabilized with two servo transducers. The f_{rep} servo changes the laser cavity length by varying the voltage across a piezoelectric via a feedback loop. The offset frequency f_0 can be altered by changing the pump laser power. The f_0 servo is connected to an acousto-optic modulator (AOM), which changes the pump laser power by using sound waves to deflect light from the pump laser via the f_0 feedback loop. Changing the pump power changes dispersion in the cavity. Due to the nonlinearity of the laser, the phase of the carrier function and thus f_0 changes.

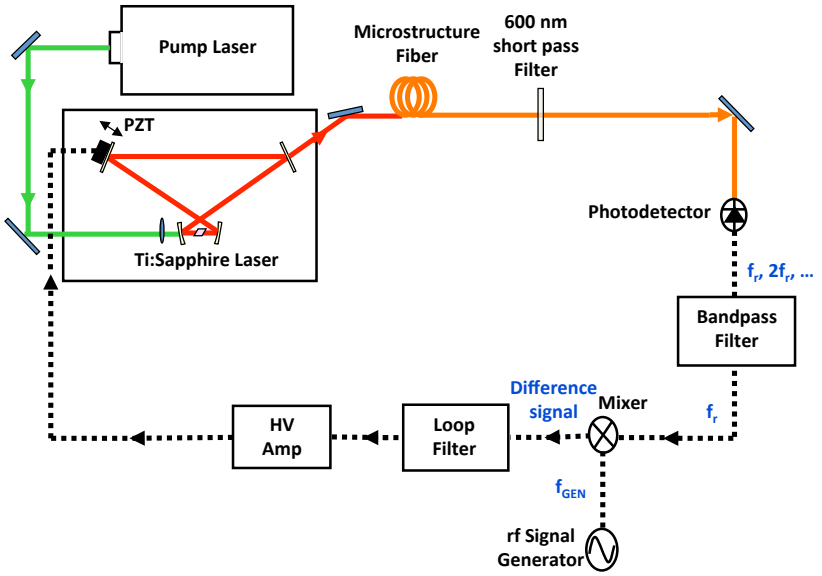

Figure 2.11: Stabilization of f_{rep} for the frequency comb in this experiment. The beat frequencies of all the different comb modes are harmonics of f_{rep}. The lowest harmonic is filtered, mixed up, conditioned in a loop filter, and fed through a high voltage amplifier to drive a piezoelectric. The piezoelectric changes the size of the cavity accordingly, thus stabilizing f_{rep}.

The repetition rate f_{rep}, which is on the order of 1 GHz for our laser, is first measured on a fast photodiode. The many modes of the comb interfere with each other to produce a series of beat frequencies that are multiples of f_{rep}. The higher harmonics are filtered out by a tunable RF filter with a range of 0.8 to 1.5 GHz and a 5% passband. The filtered signal is then mixed with an external synthesizer, which is referenced to a rubidium atomic clock. The beat signal between f_{rep} and the synthesizer is then filtered and amplified. This error signal is then fed through a loop filter, which conditions the signal such that it has high gain at low frequencies and low gain at high frequencies. This is done to avoid the natural resonance of the circuit. The conditioned signal is then fed through a high voltage amplifier as the driving voltage for a piezoelectric that changes the size of the cavity to change f_{rep} accordingly. This setup is pictured in Figure 2.11.

The stabilization of f_0 is slightly more complicated. Its stabilization setup is pictured in Figure 2.12. It requires that the comb span an optical octave, which we achieve

by sending the comb light through a microstructure fiber. The signal is then frequency doubled. The idea is to use the difference signal between the doubled frequency of multiple comb modes of index n against the comb modes of index $2n$ as an error signal, where the two frequencies are

$$\nu_1 = f_0 + nf_{rep}$$
$$\nu_2 = f_0 + 2nf_{rep}.$$

The first frequency ν_1 is frequency doubled, so that $2\nu_1 - \nu_2 = f_0$. Thus, the beat frequency between $2\nu_1$ and ν_2 is f_0, and f_0 is filtered by a bandpass filter and summed with an external synthesizer to produce a sum frequency f_{sum} that is on the order of 1.2 GHz. Unlike the process for f_{rep}, stabilizing f_0 requires mixing up the signal because f_0 is much noisier than f_{rep}. Given an f_0 with noise δf_0, the fractional noise is $\delta f_0/f_0$. When f_0 is mixed to be f_{sum}, the fractional noise is $\delta f_0/f_{sum}$, reducing the fractional noise by a factor of f_{sum}/f_0.

The sum frequency is then divided by 8 for phase-locking purposes. This process can be understood by examining the mixing process. If we mix two sinusoidal signals S_1 and S_2 at frequencies $\omega_1 = 2\pi\nu_1$ and $\omega_2 = 2\pi\nu_2$ respectively, where:

$$S_1(t) = V_1 \sin(\omega_1 t + \phi_1)$$
$$S_2(t) = V_2 \sin(\omega_2 t + \phi_2),$$

the output S_0 of the mixer is simply a product of the two signals:

$$S_0(t) = S_1(t)S_2(t) = V_1V_2 \sin(\omega_1 t + \phi_1)\sin(\omega_2 t + \phi_2). \tag{2.5}$$

A trigonometric identity tells us that this product signal is actually made of a signal at the sum frequency and difference frequency:

$$S_0(t) = \frac{1}{2}V_1V_2 \cos[(\omega_1 - \omega_2)t + (\phi_1 - \phi_2)] - \frac{1}{2}V_1V_2 \cos[(\omega_1 + \omega_2)t + (\phi_1 + \phi_2)]. \tag{2.6}$$

The sum frequency is filtered out, so we are left with

$$S_0 = \frac{1}{2}V_1V_2 \cos[(\omega_1 - \omega_2)t + (\phi_1 - \phi_2)]. \tag{2.7}$$

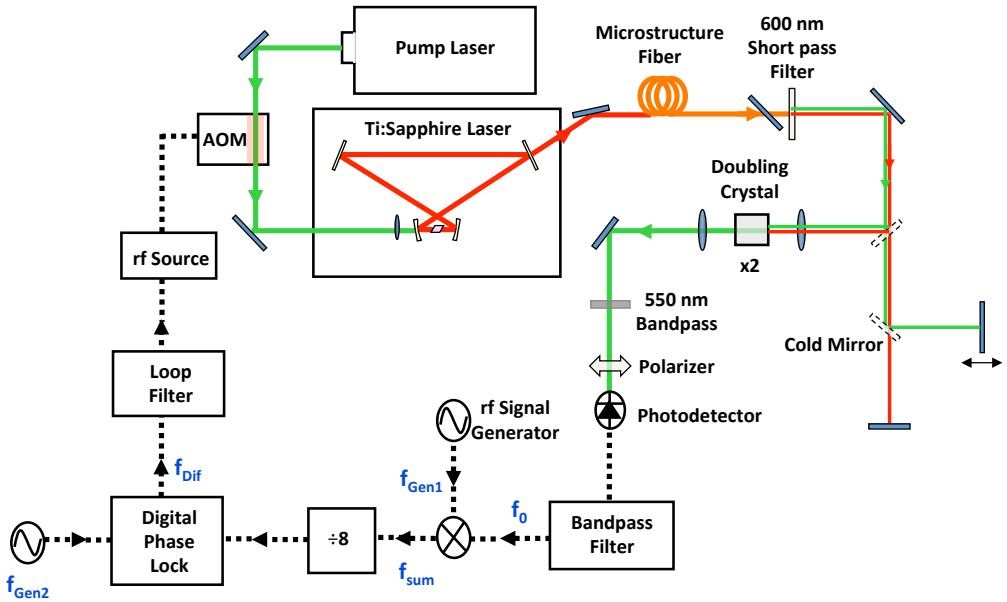

Figure 2.12: Stabilization of f_0 for the frequency comb in this experiment. The microstructure fiber broadens the comb such that it spans an octave, and the light is filtered and then frequency doubled such that the beat frequency between a mode ν_{2n} and $2\nu_n$ is f_0. The f_0 signal is then mixed down and mixed up again, conditioned with the loop filter, and then fed into an rf source that drives an AOM. The AOM changes the pump power, which changes f_0.

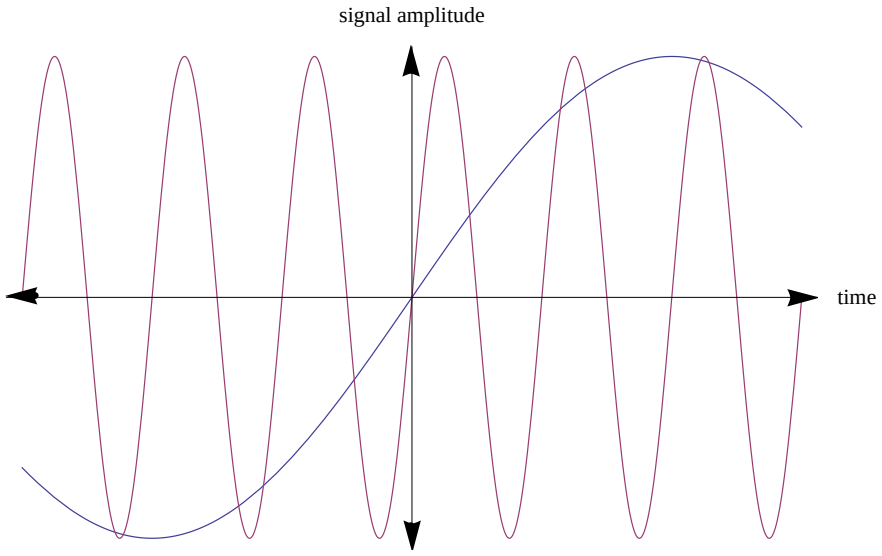

Figure 2.13: The frequency divider lengthens the period of the signal by a factor of 8, making it less likely that the phase lock will accidentally lock to an adjacent phase.

In the case of f_0 stabilization, ν_1 is $f_{sum}/8$ and ν_2 is the frequency of the synthesizer, f_{Gen2}, as pictured in Figure 2.12. To lock f_0, instead of using an error signal to match ν_1 with ν_2, the error signal is used to match ϕ_1 and ϕ_2. A phase lock rather than a frequency lock is used because phase-matching is automatically locks frequency; that is, when two waves are in phase for all time, they must also have the same frequency. The error signal is divided by 8 to prevent phase-slipping. Specifically,

$$S_{divide} = \frac{1}{2} V_1 V_2 \cos\left[\frac{1}{8}(\omega_1 - \omega_2)t + (\phi_1 - \phi_2)\right]. \tag{2.8}$$

Here it is evident that after frequency dividing, the difference in phase, $\phi_1 - \phi_2$, is much smaller compared to the size of the period, as seen in Figure 2.13. This means that it is much less likely that the phase lock will accidentally lock onto an adjacent phase.

This digital phase error signal is then sent through a loop filter and then used to determine the amplitude of a radio frequency source that drives the AOM.

Once f_0 and f_{rep} are stabilized, every comb mode can be tuned by either changing f_0 or f_{rep}. This stabilization allows for the mode frequencies of the comb to be varied so that spectroscopy can be performed. In our experiment, once the comb is frequency stabilized, we change f_{rep} by changing the synthesizer frequency to which f_{rep} is referenced, and we leave f_0 fixed.

2.5 Direct Frequency Comb Spectroscopy

Direct frequency comb spectroscopy (DFCS) directly uses the output of the frequency comb for spectroscopic experiments. It is useful for precision measurements, as it has high resolution in the time domain and can also explore fast dynamics in the frequency domain.

A stabilized frequency comb can be thought of as a laser with multiple narrow-linewidth modes at known optical frequencies. Thus, methods of cw spectroscopy can be applied to DFCS.

Single-photon DFCS is the easiest application of frequency combs to realize conceptually. A single mode of the comb is used to excite a particular atomic or molecular transition. The spectrum is recorded by detecting the fluorescence from the emission of the excited states while changing f_{rep} or f_0. However, because the total laser intensity is distributed among $\sim 10^5$ modes, the average intensity per mode is typically under 1μW. This low laser intensity, in addition to Doppler broadening from the different velocities of the sample, smears out the spectra. Doppler broadening is explained in more detail in section 3.5.2. Thus, for the best results, single-photon DFCS is often used with laser-cooled systems or atomic beams to reduce the Doppler width of the spectra.

Once spectra are obtained, the absolute frequency of a transition is determined by finding the resonant comb mode number, n. In some cases, the frequency may already be known to within half the comb mode spacing, and finding n is just a matter of plugging the known frequency into the comb equation, equation (2.1). The absolute frequency can then be calculated using the same equation with the resonant f_{rep} and f_0 values.

In the more general case, without knowing the transition in question, the absolute frequency can be determined by measuring the linecenter with two or more different f_{rep}. Assuming f_0 and f_{rep} have negligible uncertainty, the linecenter is measured with $\nu = nf_{rep} + f_0$ and then with $\nu = n(f_{rep} + \Delta f_{rep}) + (f_0 + \Delta f_0)$, where Δf_{rep} is small enough such that the resonant mode does not change. With a little algebra, it is clear that $n = -\Delta f_0/\Delta f_{rep}$. In practice, measurement uncertainty forces Δf_{rep} to be bigger, such that the mode number changes, but Δn can be determined.

This experiment uses two-photon DFCS, which has two general cases: one with an intermediate resonance, and one where the frequencies are detuned from an intermediate resonance [10]. We have set up the former case, where we excite rubidium to an intermediate state. Further details about our setup can be found in the experimental section.

3

Theoretical Discussion

In this section, we motivate the experiment by explaining the usefulness of alkali atom spectroscopy, and we discuss the different theoretical aspects of DFCS spectroscopy that were considered in our spectra calculations.

3.1 Spectroscopic notation

In this text, we will use spectroscopic notation to describe the quantum states of rubidium. The general form of the notation is $nl^{2S+1}X_J$, where n refers to the principle quantum number, l is the outermost electron configuration, S is the total spin quantum number, $2S+1$ is the number of spin states, X is a letter $S, P, D, F, ...$ that corresponds to a total electronic orbital momentum quantum number $L = 0, 1, 2, 3, ...$, respectively, and J is the total electronic angular momentum quantum number where

$$\vec{J} = \vec{L} + \vec{S}. \tag{3.1}$$

Because we will be dealing with rubidium, which is an alkali metal and thus has only one valence electron, we can simplify the notation further. Because the rest of the electrons form a closed shell, they do not contribute to the total orbital angular momentum L or spin S, and the valence electron angular momentum l is equal to the total angular momentum L. In addition, all of the states have $S = \frac{1}{2}$ from the valence electron. Thus, we can write our energy levels as nX_J without sacrificing any information.

For example, one of our energy levels of interest can be written $5d\ ^2D_{\frac{5}{2}}$, where $n = 5$, the valence electron has orbital angular momentum $l = 2$, the total orbital angular momentum $L = 2$, total spin quantum number $S = \frac{1}{2}$, $L = 2$, and total electronic angular momentum quantum number $J = \frac{5}{2}$. However, we will suppress the valence electron configuration and the spin state term and refer to the level as $5D_{\frac{5}{2}}$.

We will also refer to total nuclear spin with quantum number I and total atomic angular momentum with quantum number F, where

$$\vec{F} = \vec{I} + \vec{J}. \tag{3.2}$$

3.2 More about rubidium

The spectra of alkali metals like rubidium are exciting to study because of their relative simplicity, which makes experiment-theory comparisons more accessible. While they are multi-electron atoms, they can be modeled relatively simply because they have only one valence electron outside of a closed subshell. For all alkali metals, the total orbital angular momentum and total spin angular momentum of the core are zero, or $^1S_0$. The valence electron is bound weakly compared to the core electrons, requiring around 5 eV to detach the valence electron, whereas the least tightly bound of the core electrons requires over 20 eV [11]. Consequently, the optical spectrum arises from valence electron transitions.

At large distances, the potential in which valence electron moves approaches the Coulomb potential:

$$\lim_{r\to\infty} V(r) = -\frac{e}{4\pi\epsilon_0 r}, \tag{3.3}$$

where r is the distance between the valence electron and the nucleus. Thus, when the valence electron is in a highly excited state, where the orbitals lie largely outside of the region of the core, the orbitals approximate the hydrogen wavefunctions [11].

In addition, because alkali metals are relatively easy to understand, they are used in a variety of practical applications. Alkali atoms are used as oscillators in atomic clocks. The current SI standard for the second is defined using the oscillations between two hyperfine transitions of the ground state of cesium-133. They can also be used to make high-precision magnetometers [12].

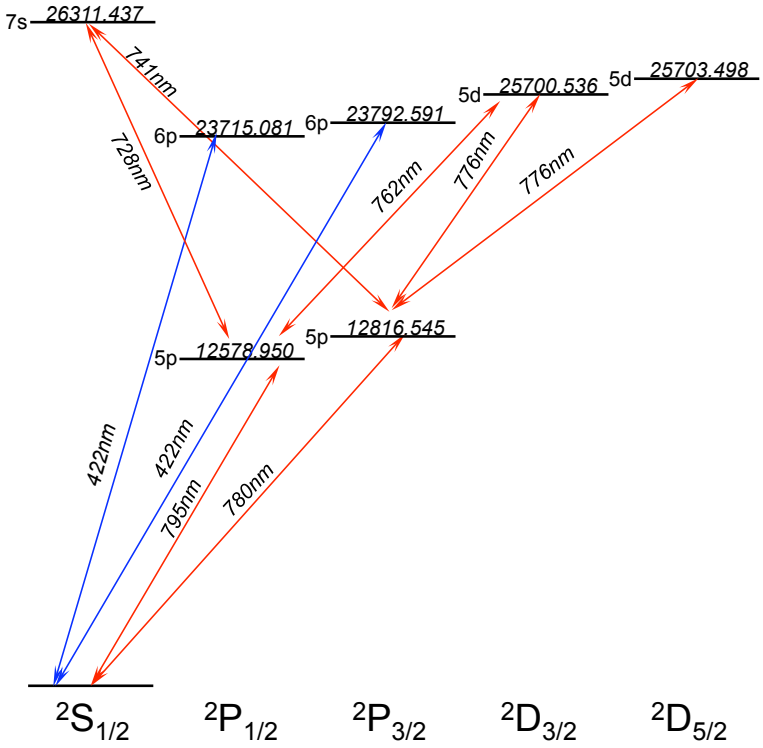

Figure 3.1: This energy level diagram includes the two-photon transitions of interest in this experiment. The two-photon transition to the 7s state was not experimentally completed but is a potential future experiment. The underlined numbers without units are wavenumbers in inverse centimeters. Wavelengths and wavenumbers are for the natural isotopic abundance of rubidium and are taken from Ref. [13].

However, while precision measurements of alkali metals have many practical applications, the primary motivation of this experiment is to demonstrate the versatility of the optical frequency comb technique for performing two-photon spectroscopy and also to investigate the interaction of atoms with resonant phase-coherent ultra-short pulses.

In this experiment, we excite two-photon transitions in rubidium from the ground state $5S_{\frac{1}{2}}$ to an intermediate state, $5P_{\frac{1}{2}}$ or $5P_{\frac{3}{2}}$, and then to a final state $5D_{\frac{3}{2}}$ or $5D_{\frac{5}{2}}$. The ground state to $5P_{\frac{1}{2}}$ transition is referred to as the D_1 transition, while the ground state to $5P_{\frac{3}{2}}$ transition is referred to as the D_2 transition. When the atom is excited to a final $5D_{\frac{3}{2}}$ state, it has a branching ratio of 0.32 to decay to the $6P_{\frac{1}{2}}$ and 0.06 branching ratio of decaying to the $6P_{\frac{3}{2}}$. The branching ratio that an excited atom in the $5D_{\frac{5}{2}}$ state will decay to the $6P_{\frac{3}{2}}$ state is 0.35 [14]. We detect these

two-photon transitions by detecting the 422 nm fluorescence from the decay of the $6P$ states to the ground state. Because the branching ratios for $5D_{\frac{5}{2}} \rightarrow 6P_{\frac{3}{2}}$ to $5D_{\frac{3}{2}} \rightarrow 6P_{\frac{1}{2}}$ *are similar, we do not include the branching ratio in our relative transition probability calculation.*

These energy levels are shown in Figure 3.1. Note that the two on-resonance transitions that take the $5S$ to $5D$ are very close in energy: the D_1 transition is at 795 nm; the D_2 transition is at 780 nm; the transition from $5P_{\frac{3}{2}}$ to either $5d$ state is 776 nm, and the transition from $5P_{\frac{3}{2}}$ to $5D_{\frac{3}{2}}$ is at 762 nm.

3.3 Fine and hyperfine splitting of energy levels

The simplest model of the rubidium atom is similar to the Bohr model of hydrogen, where the Hamiltonian only accounts for the Coulomb potential between a point-like nucleus and the valence electron and ignores spin and the higher order magnetic and electric moments of the electron and nucleus. This Coulomb-potential only Hamiltonian, called the zero-order Hamiltonian, can be further refined by including smaller interactions, which result in fine and hyperfine splitting of energy levels. These small energy splittings can be resolved by DFCS. The splittings for the different hyperfine levels in both isotopes of rubidium are shown in Figure 3.2.

3.3.1 Fine Structure

Fine structure is caused by two separate mechanisms: a relativistic effect and spin-orbit coupling. The relativistic effect can be included by replacing the classical momentum operator with the relativistic momentum operator. The full derivation of the fine structure splitting for hydrogen can be found in Ref. [15], and a more detailed explanation of fine structure splitting of alkali metals can be found in Ref. [11].

Spin-orbit coupling refers to the perturbation that arises from the proton "orbiting" around the electron in the electron's rest frame and creating a magnetic field with which the magnetic dipole moment of the electron interacts. This leads to an energy splitting that depends on the alignment of $\vec{L}$ and $\vec{S}$. In the presence of spin-orbit coupling, electronic orbital angular momentum $\vec{L}$ and electronic spin angular momentum $\vec{S}$ are not separately conserved, while total electronic angular momentum $\vec{J}$ is conserved, as pictured in Figure 3.3.

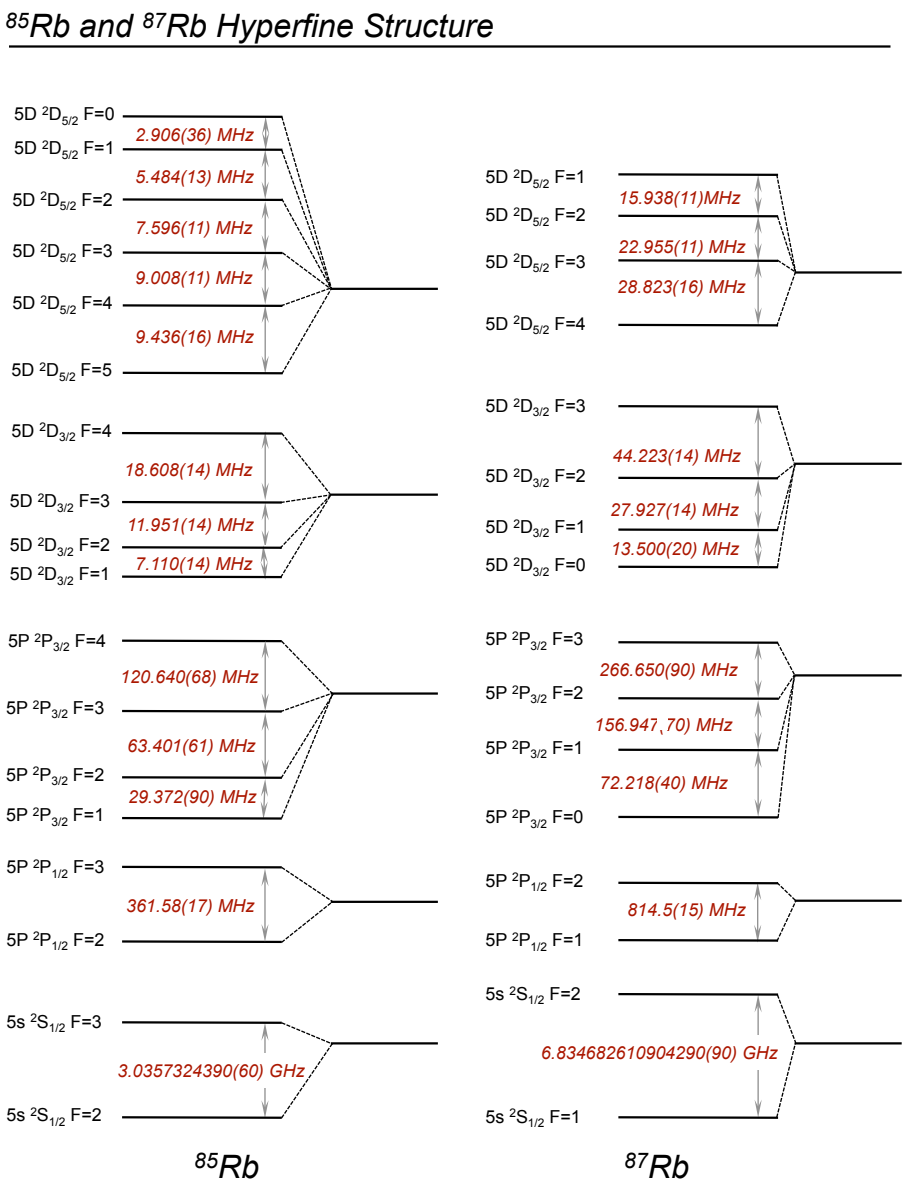

Figure 3.2: This energy level diagram includes all the hyperfine levels of our energy levels of interest for the two isotopes of rubidium. The ground state and $6P$ values are from Refs. [3, 4], and the 5D values are from Ref. [5].

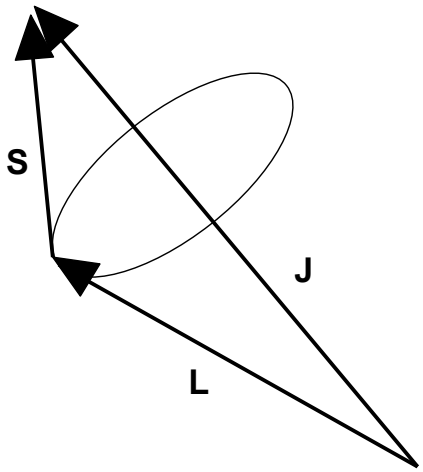

Figure 3.3: Angular momenta $\vec{S}$ and $\vec{L}$ are not separately conserved in the presence of spin-orbit coupling; they precess about fixed total electronic orbital momentum $\vec{J}$. This picture can also be extended to total atomic orbital momentum $\vec{F}$ in the presence of spin-spin coupling; in that case, $\vec{J}$ and nuclear angular momentum $\vec{I}$ are not separately conserved and precess about a fixed $\vec{F}$.

In rubidium, the fine structure splitting lifts the degeneracy between $5^2P_{\frac{1}{2}}$ and $5^2P_{\frac{3}{2}}$. This lifting of degeneracy results in a difference in energy between the $D_1(5^2S_{\frac{1}{2}} \rightarrow 5^2P_{\frac{1}{2}})$ and D_2 $(5^2S_{\frac{1}{2}} \rightarrow 5^2P_{\frac{3}{2}})$ transitions, as seen in Figure 3.1.

3.3.2 Hyperfine Structure

The rubidium Hamiltonian, after accounting for fine structure, can be even more accurately described by including higher order electric and magnetic moments of the nucleus and the electron. Hyperfine splitting arises from including the interactions of the magnetic dipole moment and the electric quadrupole moment of the nucleus. Due to symmetry, the nucleus has no electric dipole moment. Spin-spin coupling refers to the interaction of the nuclear magnetic dipole moment with the magnetic field produced by the valence electron. The splitting due to spin-spin coupling is parametrized by the magnetic dipole hyperfine coefficient A_J, and the splitting due to the electric quadrupole moment is parametrized by the electric quadrupole hyperfine coefficient B_J.

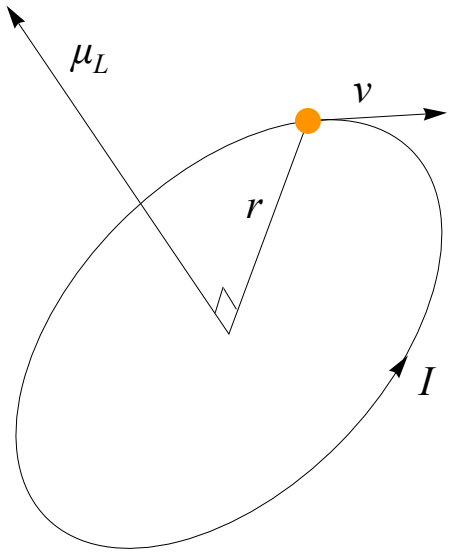

Figure 3.4: In the semiclassical model, the electron, shown as the orange dot here, orbits the nucleus. The orbiting electron can be modeled as a current loop with magnetic dipole moment μ_L. The current I points in the opposite direction of v because the electron is negatively charged. The direction of μ_L can then be found using the right-hand rule.

3.3.2.1 Hyperfine Coefficient A_J

A semiclassical approach to picturing spin-spin coupling is to model the electron as a spinning ball of charge orbiting the nucleus. From this classical picture, a magnetic field results from both the orbital angular momentum L and the intrinsic spin angular momentum S. This field then interacts with the magnetic dipole moment of the nucleus. The perturbing Hamiltonian describing this interaction can be written [16]

$$H = -\vec{\mu}_I \cdot \vec{B}_e(0), \tag{3.4}$$

where μ_I is the nuclear magnetic moment and $B_e(0)$ is the magnetic field of the valence electron at the nucleus.

The magnetic field $\vec{B}_e$ due to the valence electron is proportional to the magnetic dipole moment $\vec{\mu}_J$ of the electron. We can find $\vec{\mu}_J$ by vectorially adding the orbital magnetic moment $\vec{\mu}_L$ and spin magnetic moment $\vec{\mu}_S$, which are due to orbital angular momentum $\vec{L}$ and spin angular momentum $\vec{S}$, respectively.

In the semiclassical model, the electron orbits the nucleus, and this angular momen-

tum produces the electron magnetic dipole moment, pictured in Figure 3.4. If we first consider the orbit of the electron as a circulating current with magnitude I enclosing a plane area $d\vec{A}$, the magnetic dipole moment of the electron $\vec{\mu}_L$ is

$$\vec{\mu}_L = Id\vec{A}. \tag{3.5}$$

The current I from an electron orbiting with a velocity v in a circle of radius r is

$$I = \frac{ev}{2\pi r}, \tag{3.6}$$

where e is the elementary charge.

The area enclosed by the current is πr^2. After substituting in the angular momentum $L = mvr$ and plugging this into equation (3.5), we find

$$\mu_L = \frac{evr}{2} = \frac{eL}{2m}. \tag{3.7}$$

Because the direction of the current is opposite the direction of the electron, as the electron is negatively charged, the magnetic moment is

$$\vec{\mu}_L = -\frac{e}{2m}\vec{L}. \tag{3.8}$$

The electron magnetic moment is commonly expressed in units of the Bohr magneton μ_B [11]:

$$\vec{\mu}_L = -\frac{\mu_B \vec{L}}{\hbar}, \tag{3.9}$$

where

$$\mu_B = -\frac{e\hbar}{2m}. \tag{3.10}$$

Equation (3.9) can be generalized to a system of electrons with total orbital angular momentum $\vec{L}$ and magnetic moment $\vec{\mu}_L$ antiparallel to $\vec{L}$:

$$\vec{\mu}_L = -g_L \frac{\mu_B \vec{L}}{\hbar}. \tag{3.11}$$

Note that the actual value of $\vec{\mu}_L$ has an extra dimensionless factor g_L, which is known as the orbital angular momentum g-factor or gyromagnetic ratio and relates the

magnetic moment to the orbital angular momentum [11]. The g-factor is a constant particular to atomic state. In this case, it arises from the rubidium valence electron, and $g_L = 1$.

We can motivate that $\vec{\mu}_S$, the magnetic dipole moment due to spin, is proportional to the spin angular momentum $\vec{S}$ with a similar semiclassical description. Semiclassically, the magnetic moment $\vec{\mu}_S$ due to the spin angular momentum can be thought of as the magnetic moment of a spinning ball of charge. The magnetic moment of a spinning ball of charge can be calculated by integrating the moments of many current loops. Similar to equation (3.11), $\vec{\mu}_S$ can be written [11]

$$\vec{\mu}_S = -g_S \frac{\mu_B \vec{S}}{\hbar}, \tag{3.12}$$

where $\vec{S}$ is the spin angular momentum of the electron, and g_S is the spin angular momentum g-factor. The g_S factor for an electron is approximately 2.

We can now find the total magnetic moment produced by the electron, $\vec{\mu}_J$, by adding $\vec{\mu}_L$ from (3.11) and $\vec{\mu}_S$ from (3.12) [16]

$$\vec{\mu}_J = -\frac{\mu_B}{\hbar}(g_L \vec{L} + g_S \vec{S}). \tag{3.13}$$

For an electron, $g_L = 1$ and $g_S = 2$ [17]:

$$g_L \vec{L} + g_S \vec{S} = \vec{L} + 2\vec{S}. \tag{3.14}$$

Because $\vec{J} = \vec{L} + \vec{S}$, we have

$$\vec{L} + 2\vec{S} = \vec{J} + \vec{S}. \tag{3.15}$$

The vector $\vec{S}$ can be thought of as the projection of $\vec{S}$ along $\vec{J}$ [18]:

$$\vec{S} = \frac{\langle \vec{S} \cdot \vec{J} \rangle}{J(J+1)} \vec{J} \tag{3.16}$$

and using the relations

$$\langle \vec{S} \cdot \vec{J} \rangle = \langle \vec{S} \cdot (\vec{S} + \vec{L}) \rangle = \langle \vec{S}^2 \rangle + \langle \vec{S} \cdot \vec{L} \rangle \tag{3.17}$$

$$\langle \vec{S}^2 \rangle = S(S+1) \tag{3.18}$$

$$\vec{J}^2 = \vec{L}^2 + \vec{S}^2 + 2\vec{S} \cdot \vec{L} \tag{3.19}$$

and rearranging (3.19), we get

$$\vec{S} \cdot \vec{L} = \frac{1}{2}(\vec{J}^2 - \vec{L}^2 - \vec{S}^2). \tag{3.20}$$

Plugging this into (3.17),we find

$$\langle \vec{S} \cdot \vec{J} \rangle = \frac{1}{2}((J(J+1) + S(S+1) - L(L+1)). \tag{3.21}$$

Combining (3.21) and (3.16), we find

$$\vec{S} = \frac{J(J+1) + S(S+1) - L(L+1)}{2J(J+1)} \vec{J}. \tag{3.22}$$

Adding $\vec{J}$ and $\vec{S}$, we get

$$\vec{J} + \vec{S} = \left(1 + \frac{J(J+1) + S(S+1) - L(L+1)}{2J(J+1)}\right) \vec{J} \tag{3.23}$$

Thus, referring back to equation (3.13), we can say that

$$g_L \vec{L} + g_S \vec{S} = \left(1 + \frac{J(J+1) + S(S+1) - L(L+1)}{2J(J+1)}\right) \vec{J}, \tag{3.24}$$

or more compactly,

$$g_J \vec{J} = g_L \vec{L} + g_S \vec{S}. \tag{3.25}$$

The factor in front, g_J, is known as the Landé g-factor, where [17]

$$g_J = 1 + \frac{J(J+1) - L(L+1) + S(S+1)}{2J(J+1)}, \tag{3.26}$$

and now, it is clear from equation (3.13) that the electron magnetic moment μ_J is proportional to $\vec{J}$:

$$\vec{\mu}_J = -\frac{\mu_B}{\hbar} g_J \vec{J}. \tag{3.27}$$

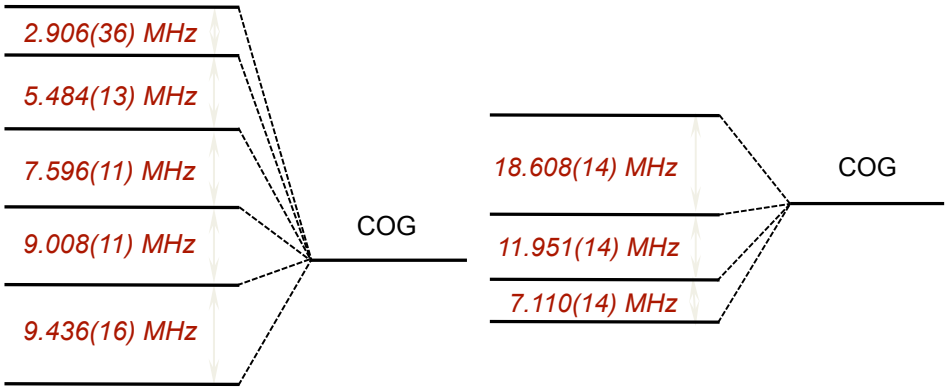

(a) The hyperfine splitting in $5^2D_{\frac{5}{2}}$ **(b)** The hyperfine splitting in $5^2D_{\frac{3}{2}}$

Figure 3.5: Hyperfine Energy Splitting - For rubidium-85, $I = \frac{5}{2}$. In (a), $J = \frac{5}{2}$, and in (b), $J = \frac{5}{2}$. COG stands for center of gravity frequency, which are the eigenstates of the Hamiltonian if fine structure is included but hyperfine structure is ignored. Frequencies found in Ref. [3].

The nuclear magnetic moment $\vec{\mu_I}$ is given by

$$\vec{\mu}_I = g_I \mu_n \vec{I} \tag{3.28}$$

where g_I is the nuclear gyromagnetic ratio and μ_n is the nuclear magneton, defined by

$$\mu_n = \frac{e\hbar}{2m_p}, \tag{3.29}$$

where m_p is the mass of proton, e is the elementary charge, and $\hbar$ is the reduced Planck constant. The nuclear magneton is a constant used as a convenient unit of nuclear magnetic moment that is analogous to the Bohr magneton's role in expressing electron magnetic moment.

Thus, we can see from equations (3.27) and (3.28) that the perturbing Hamiltonian (3.4) can be written

$$H = A_J(\vec{I} \cdot \vec{J}) \tag{3.30}$$

We can rewrite equation (3.30) using

$$\vec{I} \cdot \vec{J} = \frac{1}{2}(\vec{F^2} - \vec{J^2} - \vec{I^2}), \tag{3.31}$$

which is analogous to equation (3.20), and have

$$H = \frac{A_J}{2}(\vec{F}^2 - \vec{J}^2 - \vec{I}^2), \tag{3.32}$$

where F is the total atomic angular momentum. If we define κ as

$$\kappa = F(F+1) - I(I+1) - J(J+1), \tag{3.33}$$

then the energy difference ΔE between and unperturbed energy level and a hyperfine level with total angular momentum F is

$$\Delta E = \frac{A_J}{2}\kappa \tag{3.34}$$

Thus, for an energy level with given J and I, the energy levels split according to the different values of F. The possible values of F can be found by adding angular momenta J and I quantum mechanically and range from $F = |J - I|, \ldots, J + I$.

3.3.2.2 Hyperfine Coefficient B_J

A smaller contribution to the hyperfine perturbation Hamiltonian arises from the electric quadrupole moment of the nucleus. The electrostatic interaction between a proton at point $\vec{r}_n$ and an electron at point $\vec{r}_e$ is given by

$$H_2 = -\frac{e^2}{4\pi\epsilon_0|\vec{r}_e - \vec{r}_n|} \tag{3.35}$$

If we take $r_e > r_n$, equation (3.35) can be expanded into powers of r_n/r_e:

$$\begin{aligned} H_2 &= -\frac{e^2}{4\pi\epsilon_0}(r_e^2 + r_n^2 - 2r_e r_n \cos\theta_{en})^{1/2} \\ &= -\frac{e^2}{4\pi\epsilon_0}\sum_k \frac{r_n^k}{r_e^{k+1}} P_k(\cos\theta_{en}), \end{aligned} \tag{3.36}$$

where $P_k(\cos\theta_{en})$ is the Legendre polynomial of order k and θ_{en} is the angle between $\vec{r}_e$ and $\vec{r}_n$ as shown in Figure 3.6. Here the first term of the summation is the electrostatic monopole term, the second is the dipole term, and the third is the electric quadrupole term of the nucleus. The nucleus has no electric dipole moment nor any other higher order moments of odd order.

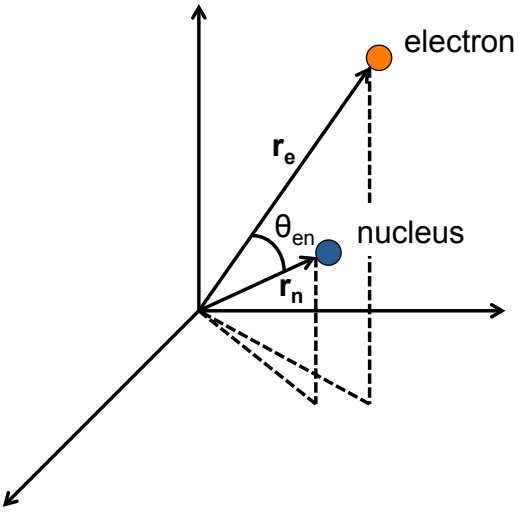

Figure 3.6: The definition of the angles θ_{en}, vectors $\vec{r}_n$ and $\vec{r}_e$, used in the multipole expansion in equation 3.36.

It can be shown that the electric quadrupole interaction can be written in the form [16]

$$H_2 = -\frac{B_J}{2I(2I-1)J(2J-1)}\left[3(\vec{I}\cdot\vec{J})^2 + \frac{3}{2}(\vec{I}\cdot\vec{J}) - I(I+1)J(J+1)\right], \tag{3.37}$$

where B_J is the electric quadrupole interaction constant defined by

$$B_J = eQ\left\langle \frac{\partial^2 V_e}{\partial z^2} \right\rangle. \tag{3.38}$$

Here the quantity $\langle \partial^2 V_e/\partial z^2 \rangle$ is the average field gradient at the nucleus.

If we include the electric quadrupole interaction in addition to the nuclear magnetic dipole interaction, we find the energy splitting between an fine structure energy level with given electronic angular momentum quantum number J and a hyperfine level with total angular momentum F,

$$\Delta E = \frac{A_J}{2}\kappa + \frac{B_J}{8I(2I-1)J(2J-1)}\left[3\kappa(\kappa+1) - 4I(I+1)J(J+1)\right] \tag{3.39}$$

For more details, see Refs. [16, 17].

3.4 Isotope Shifts

The energy levels of the different isotopes of any element are shifted relative to one another. These shifts arise because of the differences in the nuclei of the isotopes, which alter the electric and magnetic moments of the nucleus. For example, a larger isotope will have more neutrons, and thus have a larger nuclear radius and mass. In addition, the difference of the shapes of the nuclei of two isotopes can lead to an isotope shift [17].

Rubidium has one stable isotope, ^{85}Rb, and a weakly radioactive isotope, ^{87}Rb, with a half-life of over ten billion years, and is thus effectively stable. The transition frequencies of ^{87}Rb are shifted slightly up compared to those of ^{85}Rb. The natural abundance of ^{85}Rb is 72.17(2)%, and the natural abundance of ^{87}Rb is 27.83(2)% [4]. Both isotopes are assumed to be present in their natural abundance in the vapor cell used in this experiment.

3.5 The Character of Spectral Lines

The shape of spectral lines result from both inherent characteristics of the atom and also from the conditions under which the spectra were measured. In this section, we explore both homogeneous and inhomogeneous broadening. Processes that have the same effect on all atoms in the sample, such as power broadening, are known as *homogeneous broadening* mechanisms. On the contrary, broadening mechanisms that vary from one atom to another, such as Doppler broadening, are known as *inhomogeneous broadening* mechanisms.

In this section, we will discuss the natural line width and Doppler broadening and briefly qualitatively explain pressure broadening, power broadening, and transit broadening in spectral lines.

3.5.1 Natural Line Width

Even with the highest resolution spectrometers, spectral lines are never infinitely sharp. By the time-energy uncertainty relation, they have an uncertainty dependent on the mean lifetime of the transition. Instead, the observed spectral line has a spectral distribution $I(f)$ centered about a central frequency $f_0 \alpha \Delta E$, where $\Delta E = E_2 - E_1$,

which is the energy of its corresponding transition, where E_2 and E_1 are the energies of the upper and lower energy levels, respectively. The function describing the intensity of the transition in the vicinity of f_0 is called the *line profile*. The line profile of a transition for a two-level system follows a Lorentzian distribution [19]:

$$I(\omega) = I_0 \frac{\gamma/(2\pi)}{(\omega - \omega_0)^2 + (\gamma/2)^2} \tag{3.40}$$

where γ corresponds to the full width at half maximum (FWHM) of the Lorentzian, I_0 is proportional to the amplitude of the peak intensity, ω_0 is the angular frequency corresponding to $2\pi f_0$. Henceforth, ω will be used to denote angular frequencies to avoid writing extra factors of 2π.

Generally, the FWHM γ is known as the *homogeneous linewidth* and arises from different homogeneous line broadening mechanisms, such as pressure broadening, power broadening, and the natural linewidth. The minimum γ predicted by the uncertainty principle is the natural linewidth. The uncertainty principle says

$$\Delta E \, \Delta t \geq \hbar. \tag{3.41}$$

Let τ equal the mean lifetime of the transition. If $\gamma = 1/\tau$, then

$$\Delta E \, \Delta t = \hbar \, \Delta\omega \, \tau = \hbar \, \gamma \, \tau = \hbar. \tag{3.42}$$

Equation 3.40 can be generalized to a multi-level atom. For a level k, the half-width Γ of the spectral line is determined by its radiative lifetime [16]:

$$\Gamma_k = \Delta\omega_k = \Delta E_k/\hbar = 1/\tau_k = \sum_i A_{ki}, \tag{3.43}$$

where A_{ki} are the transition rates of all the electric dipole transitions from level k to lower levels i. The transition probability is directly proportional to the transition rate, which is the inverse of the transition lifetime τ_{ki}. The line profile of the transition from level $|k\rangle \rightarrow |i\rangle$ can be written

$$I_{ki}(\omega) = I_0 \frac{\Gamma/(2\pi)}{(\omega - \omega_{ki})^2 + (\Gamma/2)^2} \, . \tag{3.44}$$

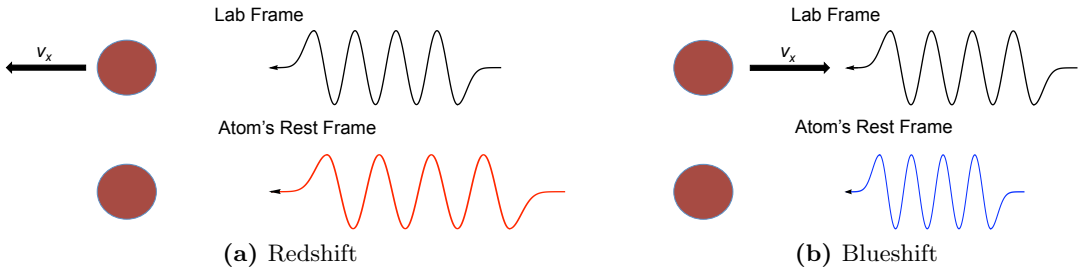

(a) Redshift **(b)** Blueshift

Figure 3.7: Due to the Doppler effect, frequencies are redshifted if the atom is moving away from the photon, and frequencies are blueshifted if the atom is moving towards the photon. Consequently, because a sample of atoms follows the Maxwell-Boltzmann distribution, the atoms will be on-resonance with a range of frequencies. This effect smears out the spectrum and is called *Doppler broadening*.

3.5.2 Doppler Broadening

The spectra of a sample of atoms also exhibits Doppler broadening, which is a type of inhomogeneous broadening. For a sample of atoms at temperature T, the velocity distribution of the atoms follows the Maxwell-Boltzmann distribution.

Let a photon at frequency ω_0 be emitted in a stationary observer's reference frame. An atom that is moving with nonrelativistic velocity $\vec{v}$ relative to the observer sees ω_0 as [16]

$$\omega = \omega_0 \left(1 - \frac{\vec{v} \cdot \hat{\mathbf{r}}}{c}\right) = \omega_0 - \vec{k} \cdot \vec{v} \tag{3.45}$$

where $\hat{\mathbf{r}}$ is a unit vector with positive direction moving away from the observer, as pictured in Figure 3.7. Here $\vec{k}$ is the wave vector of the light with magnitude defined as $2\pi/\lambda$, where λ is the wavelength of the light.

This shows that resonance occurs at different frequencies for atoms at different velocities, thus broadening the spectral line. This effect particularly hinders precision measurement, and many techniques can be used to avoid Doppler broadening, including laser cooling and trapping. This experiment largely avoids Doppler broadening by using velocity selective resonance by counterpropagating two beams at the vapor cell, explained in section 3.7.

3.5.3 Other Types of Broadening

Some other types of line broadening include pressure broadening, power broadening, and transit broadening.

Pressure broadening arises from the perturbing forces from neighboring atoms, electrons or ions. For example, the presence of other particles may create collisional shifts in the energy levels. In this experiment, pressure broadening is negligible because we are able to control the density of the atoms in the vapor cell by changing the temperature of the cell. A trade-off exists between increasing of atoms in the rubidium vapor to increase signal size and limiting the pressure broadening.

When the laser light field itself perturbs the energy levels of the atomic states significantly, power broadening occurs. A rigorous treatment of power broadening can be found in Ref. [20].

We can show that power broadening is insignificant in this experiment by measuring the intensity of the light from the interference filters and estimating the number of modes contained in that light.

Using the relation

$$d\lambda = -\frac{\lambda^2}{c} df, \tag{3.46}$$

where $df = f_{rep}$, which is on the order of 900 MHz, we find that when λ=700 nm, $d\lambda$ is about 1.5×10^{-12} m, and a 20 nm passband contains on the order of $\sim 10,000$ modes.

The power of the comb near that frequency over a 20 nm passband was measured to be on the order of 500 μW. Assuming equal power for each of the modes, each mode has an power of about 50 nW. Our beam size is focused to a radius of about 100 μm, which means each mode has an intensity of 500 μW/cm^2. The saturation intensity for the D_2 transition in rubidium is 1.64 mW/cm^2 [21]. Our intensity is about a third of that limit, and thus, power broadening is insignificant.

Transit broadening occurs as laser beams are focused more tightly. When beams are focused, their intensity increases, which will increase the transition probability, explained in Section 3.6. However, there is a trade-off: as the laser beam focuses tighter, the spectral line broadens. To gain a qualitative picture, let us have an atom with some velocity cross a laser beam. The more focused the beam, the shorter the time the atom spends in the beam. In the atom's reference frame, it is as though the atom observes a pulse of light. From the time-energy uncertainty principle, this means that the atom will observe a range of frequencies, making off-resonance laser beams more likely to cause a transition, and thus broadening the spectral line. Thus, once the

beam size is small enough such that the linewidth broadens, decreasing the beam size further will not improve the measurement.

3.6 Transition Probabilities

When an atom is in any stationary state with no external perturbations, it will stay in that state forever. But no atom, in the lab or at large, is wholly isolated from external electric and magnetic fields, and these perturbations cause transitions between stationary states.

The differential transition rate W_{fi} from initial state $|i\rangle$ to final state $|f\rangle$ is given by Fermi's golden rule:

$$W_{fi} = \frac{2\pi}{\hbar}|\langle f|H'|i\rangle|^2 \rho_f(E)P(E)dE, \tag{3.47}$$

where ρ_f is the density of states, or number of states per unit energy, $P(E)$ is the distribution of energies that allow a transition to occur, and H' is the perturbing Hamiltonian [20]. For an atom in an external electromagnetic field, as is the case of this experiment, the perturbing Hamiltonian is the dipole operator $\hat{\mathbf{d}} = e\hat{\mathbf{r}}$, where e is the elementary charge and $\hat{\mathbf{r}}$ is the position vector.

Thus, the transition probabilities can be calculated by finding the matrix elements of the electric dipole operator $\hat{\mathbf{d}}$.

Two-photon transitions arise from second-order perturbation theory. The two-photon transition probability P from the $5S_{1/2}$ ground state to a final state $|n''L''_{J''}F''\rangle$ is given by [22]:

$$P(5S_{1/2}F, n''L''_{J''}F'') \;\alpha\; \frac{1}{2F+1}\frac{I_1 I_2}{\left[\omega_{5S_{1/2}F:n''L''_{J''}F''} - (\omega_1 + \vec{k}_1\cdot\vec{v}) - (\omega_2 + \vec{k}_2\cdot\vec{v})\right]^2 + \left(\frac{\gamma_{n''L''_{J''}}}{2}\right)^2} \times \sum_{M_F, M_{F''}} \left| \sum_{F', M_{F'}} \frac{\langle n''L''_{J''}F''M''_F|\hat{\mathbf{e}}_2\cdot\vec{d}|5P_{J'}F'M'_F\rangle\langle 5P_{J'}F'M'_F|\hat{\mathbf{e}}_1\cdot\vec{d}|5S_{1/2}FM_F\rangle}{\omega_{5S_{1/2}F:5P_{J'}F'} - (\omega_1 + \vec{k}_1\cdot\vec{v}) - \frac{i\gamma_{5P_{J'}}}{2}} \right|^2 . \tag{3.48}$$

Here, $\omega_{A:B}$ is the resonant angular frequency from state A to state B; M_F, M'_F, and M''_F are the projections of the total atomic angular momenta F, F', and F'' along the axis of quantization; $I_{1(2)}$ is the intensity of the first (second) beam; $\omega_{1(2)}$ are the frequencies of the first (second) photon; $\vec{v}$ is the velocity of the atom; $\vec{k}_{1(2)}$ is the wave vector for the first (second) photon; $\hat{\mathbf{e}}_{1(2)}$ is the unit vector along the direction of the axis of quantization for the first (second) laser beam; $\vec{d}$ is the electric dipole operator; γ_{nL} is the homogeneous linewidth of the state $|nL_J\rangle$.

The second term in second line of the equation (3.48) demonstrates that the photon transition can occur when no intermediate resonance occurs, as long as energy is conserved. Specifically, for a given linewidth $\gamma_{n''L''_{J''}}$, when the Doppler-shifted frequency of the first photon, $(\omega_1+\vec{k}_1\cdot\vec{v})$, and the Doppler-shifted frequency of the second photon, $(\omega_2+\vec{k}_2\cdot\vec{v})$, add to equal the total frequency of the transition $\omega_{5S_{1/2}F:5P_{J'}F'}$, the term is maximized.

The second term shows the contribution of an intermediate resonance state $5P_{J'}$ to the two-photon transition probability. For a given linewidth $\gamma_{5P_{J'}}$, when the Doppler-shifted frequency of the first photon, $(\omega_1+\vec{k}_1\cdot\vec{v})$, equals the frequency of the transition to the intermediate state, $\omega_{5S_{1/2}F:5P_{J'}F'}$, the second term is maximized. This indicates that the transition is greatly amplified when the intermediate resonance state occurs.

Note also that the transition probability scales to the product of the intensities of the two beams. Thus, to increase the transition probability, we focus the beam as tightly as we can without causing too much transit broadening.

However, calculating the absolute transition probabilities using equation (3.48) is difficult; it involves finding many, many matrix elements of the dipole operator $\hat{\mathbf{d}}$. Thus, in our spectra calculations, discussed in 5.1, we used several theoretical techniques to calculate relative transition probabilities. In the following sections, we explain these techniques for calculating the relative transition probabilities of the two-photon transitions in this experiment.

3.6.1 Clebsch-Gordan Coefficients

Before we dig into the meat of calculating relative transition probabilities, it is necessary to understand the quantum mechanical addition of angular momenta. A full explanation of angular momenta addition can be found in Ref. [15, 23] and will not

be discussed in detail here. The focus of this section is to explain the relevance of Clebsch-Gordan coefficients to angular momentum addition and basis transformations.

Given two states with angular momentum quantum numbers j and κ with corresponding magnetic quantum numbers m and q, respectively, the combined state $|j', m'\rangle$ will be a linear combination of the composite state $|j, m\rangle|\kappa, q\rangle$, where $j' = j + \kappa$:

$$|j', m'\rangle = \sum_{m+q=m'} \langle j, m, \kappa, q|j', m'\rangle |j, m\rangle|\kappa, q\rangle \tag{3.49}$$

The factor $\langle j, m, \kappa, q|j', m'\rangle$ is known as the Clebsch-Gordan coefficient, and because of the tediousness of its calculation, usually is found in a table. In other words, the Clebsch-Gordan coefficients determine the basis transformation from the $|j', m'\rangle$ basis that couples j and κ to a basis where j and κ are uncoupled, $|j, m\rangle|\kappa, q\rangle$.

Clebsch-Gordan coefficients can also be written in terms of the Wigner 3-j symbol:

$$\langle j, m, \kappa, q|j', m'\rangle = (-1)^{j-\kappa+m'} \sqrt{2j+1} \begin{pmatrix} j & \kappa & j' \\ m & q & -m' \end{pmatrix}, \tag{3.50}$$

where the matrix on the right-hand side is referred to as the 3-j symbol. The use of the 3-j symbol is often preferred over the Clebsch-Gordan coefficient for symmetry reasons, but the two contain the same physical information.

The Clebsch-Gordan coefficients are used in the Wigner-Eckart theorem, which is used to calculate transition probabilities, explained in the next section.

3.6.2 Wigner-Eckart Theorem

The calculation of matrix elements of tensor operators between two angular momentum eigenstates is ubiquitous in atomic physics. The Wigner-Eckart theorem is an oft-invoked tool for simplifying the calculation of these matrix elements. In this section we emphasize the utility of the theorem rather than its proof. The formal proof can be found in Ref. [23].

Given two electronic states $|\xi, j, m\rangle$ and $|\xi', j', m'\rangle$, where j is an angular momentum quantum number, m is its corresponding magnetic quantum number, designating the component of j in the z-direction, and ξ represents all other quantum numbers, the Wigner-Eckart Theorem allows the matrix element of an irreducible tensor operator T^q_κ

between these two states to be written

$$\langle \xi', j', m' | T_q^\kappa | \xi, j, m \rangle = \frac{(\xi', j' || T^\kappa || \xi, j)}{\sqrt{2j'+1}} \langle j, m, \kappa, q | j', m' \rangle. \tag{3.51}$$

Here, j constitutes an angular momentum quantum number, m is its magnetic quantum number, κ is the rank of the tensor operator, and q is the spherical component of the tensor operator. In this general case, κ is not angular momentum, but it is analogous to angular momentum, and the Clebsch-Gordan coefficient can be found by the addition of κ and j as angular momenta. Irreducible tensor operators are explained in Ref. [20].

We can see that the matrix element on the left hand side of equation (3.51) can be written as the product of two factors. The numerator of the first factor, $(\xi', j' || \hat{\mathbf{d}} || \xi, j)$, is called the *reduced matrix element* and is a property of the particular physical observable in question and is independent of magnetic quantum numbers. The second factor, $\langle j, m, \kappa, q | j', m' \rangle$ is the Clebsch-Gordan coefficient for adding angular momenta j and κ to get j'.

The significance of the Wigner-Eckart theorem lies in the convenience that results from factoring the matrix element. The Clebsch-Gordan coefficient is dependent only on the geometry of the system, that is, the orientation of the system with respect to the z-axis, and is entirely independent of any reference to the particular tensor operator. This means that if the reduced matrix element for a particular j and κ is known, then all the matrix elements are known for all the combinations of m, q, and m', because all the matrix elements of all the different combinations of q, m, m' are proportional to each other via the Clebsch-Gordan coefficients.

Transition probabilities are proportional to the matrix elements, which means that the Wigner-Eckart theorem makes relative transition probabilities between energy levels with the same j and κ trivial: they are related by the ratio of their Clebsch-Gordan coefficients [20].

3.6.3 Relative Transition Probabilities

Take a three-level system similar to the energy levels in our experiment, with multiple hyperfine F levels in the ground state $|1\rangle$, intermediate state $|2\rangle$, and final state $|3\rangle$.

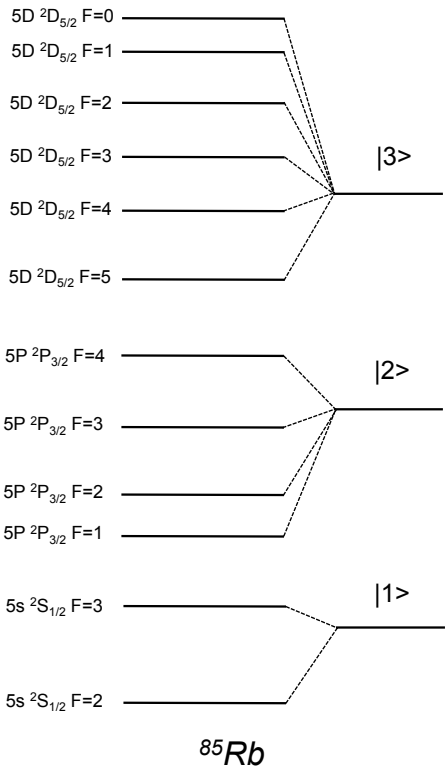

Figure 3.8: An example of a three-level system in rubidium with multiple hyperfine levels in $|1\rangle$, $|2\rangle$, and $|3\rangle$.

We can now apply the Clebsch-Gordan coefficient basis transformation technique in Section 3.6.1 and the Wigner-Eckart theorem to determine the relative transition probabilities between the different hyperfine levels in the $|1\rangle$ to the $|2\rangle$ and similarly to the transition probabilities of the hyperfine levels in the $|2\rangle$ to the $|3\rangle$. We apply the uncoupled-to-coupled basis transformation stated in equation (3.49) to the angular momentum eigenstates $|J, I, F, M_F\rangle$. In other words,

$$|J, I, F, M_F\rangle = \sum_{M_I+M_J=M_F} \langle J, M_J, I, M_I|F, M_F\rangle \, |J, M_J\rangle \, |I, M_I\rangle, \tag{3.52}$$

where $\langle J, M_J, I, M_I|F, M_F\rangle$ is the appropriate Clebsch-Gordan coefficient, and we have transformed the right-hand side into a linear combination of the uncoupled basis states, $|J, M_J\rangle \, |I, M_I\rangle$.

$$|J, I, F, M_F\rangle = \sum_{M_I+M_J=M_F} \langle J, M_J, I, M_I|F, M_F\rangle \, |J, M_J\rangle \, |I, M_I\rangle, \tag{3.53}$$

We can uncouple the basis further by transforming the left hand side of equation 3.52 into the L basis.

For a given light polarization in the spherical basis q, the matrix elements for different magnetic sublevels is given by

$$\begin{aligned}
&\langle n'L'_{J'}F'M'_F|d_q|nL_JFM_F\rangle \\
&\qquad = (-1)^{F'-M'_F}(-1)^{S+1+L'+J'} \begin{pmatrix} F' & 1 & F \\ -M'_F & q & M_F \end{pmatrix} (n'L_{J'}F'||d||nL_JF) \\
&\qquad = (-1)^{F'+M'_F+I+1+J+F}\sqrt{(2F+1)(2F'+1)} \\
&\qquad\quad \times \begin{pmatrix} F' & 1 & F \\ -M'_F & q & M_F \end{pmatrix} \begin{Bmatrix} J' & F' & I \\ F & J & 1 \end{Bmatrix} (n'L_{J'}||d||nL_J)
\end{aligned} \tag{3.54}$$

Here the matrix in the parentheses is the Wigner $3j$ symbol, and the term in curly braces is known as a *Wigner 6j* symbol.

The hyperfine levels for $|1\rangle$ all have the same J, and similarly do the hyperfine levels of $|2\rangle$ and $|3\rangle$. This means all the transitions between the different hyperfine levels of $|1\rangle$ and the different hyperfine levels of $|3\rangle$ can be related by the ratio of their $3j$ symbols. Similarly, relative transition probabilities can also be calculated between

different transitions with the same L. For example, the relative transition probabilities of the D_1 and D_2, which have the same L, have the same reduced matrix element and can be calculated using this relation.

3.7 Velocity Selective Resonance

The use of vapor cells, while simple and cheap to manufacture, is prone to many complications in precision spectroscopy. One of the problems is Doppler broadening, explained in Section 3.5.2. We largely avoid Doppler broadening by exploiting a technique called velocity selective resonance.

Regarding the same three levels as in the previous section, from conservation of energy, the two-photon transition can only be made if the sum of the energies of the two photons is equal to the sum of the spacing of the two energy levels, or,

$$\nu_{|1\rangle\rightarrow|3\rangle} = \nu_{1\gamma} + \nu_{2\gamma} \tag{3.55}$$

where $\nu_{|1\rangle\rightarrow|3\rangle}$ is the total frequency spacing between $|1\rangle$ and $|3\rangle$, and $\nu_{1\gamma}$ and $\nu_{2\gamma}$ are the frequencies of the two photons, respectively.

The transition rate from $|1\rangle \rightarrow |3\rangle$ is highest when the first photon excites the atom to an intermediate state, as explained in Section 3.6. While transitions without an intermediate resonance state are possible, their probability is significantly lower than transitions with an intermediate resonance state. Thus, we will focus on these on-resonance transitions.

Let us counterpropagate two laser beams horizontally at the rubidium vapor cell along our x-axis, shown in Figure 4.5. These two beams contain the comb modes that are passed by their respective interference filters. Let's call the two nearest-resonant modes from each of the counterpropagating beams ν_1 and ν_2. From the comb equation,

$$\nu_1 = f_0 + n_1 f_{rep} \tag{3.56}$$

$$\nu_2 = f_0 + n_2 f_{rep} \tag{3.57}$$

But because the atom has a velocity $\vec{v}$, it will see the incoming photon at frequency ν_1 and its counterpropagating counterpart at ν_2 at Doppler shifted frequencies ν_1' and ν_2',

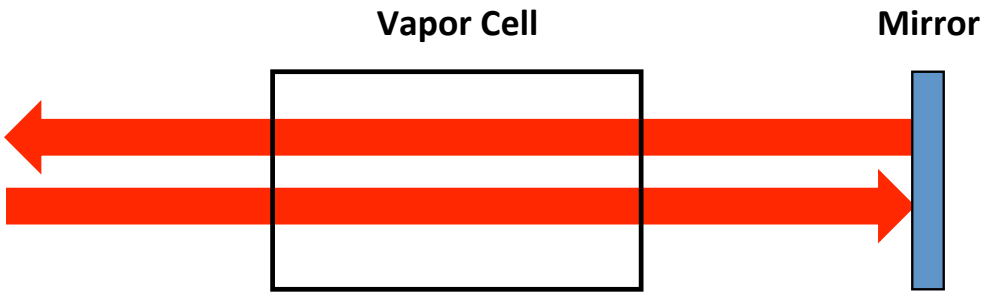

Figure 3.9: The photons γ_1 and γ_2 are counterpropagating parallel and antiparallel to the x-axis. The rubidium atoms have a velocity distribution given by Maxwell-Boltzmann statistics. A single velocity class, which contains all the atoms whose x-component velocity is v_x, will see one photon redshifted the same amount as the other photon is blueshifted.

respectively:

$$\nu_1' = \nu_1 \left(1 - \frac{v_x}{c}\right) \tag{3.58}$$

$$\nu_2' = \nu_2 \left(1 + \frac{v_x}{c}\right) \tag{3.59}$$

where v_x is the component of $\vec{v}$ along the x-axis.

The on-resonance two-photon transition can only occur when both of the Doppler-shifted frequencies equal the transition frequencies at the same time:

$$\nu_{|1\rangle\rightarrow|2\rangle} = \nu_1' = (f_0 + n_1 f_{rep}) \left(1 - \frac{v}{c}\right) \tag{3.60}$$

$$\nu_{|2\rangle\rightarrow|3\rangle} = \nu_2' = (f_0 + n_2 f_{rep}) \left(1 + \frac{v}{c}\right) \tag{3.61}$$

and the resonance conditions become

$$\nu_{|1\rangle\rightarrow|3\rangle} = \left[n_1 + n_2 + \frac{v}{c}(n_1 - n_2)\right] f_{rep} + 2f_0 \tag{3.62}$$

$$\nu_{|1\rangle\rightarrow|2\rangle} = (n_1 f_{rep} + f_0) \left(1 + \frac{v}{c}\right) \tag{3.63}$$

For a given pair of comb modes n_1 and n_2 and a fixed value of f_0, a unique f_{rep} and v exist such that the resonance condition is satisfied. When we scan the comb through a range of f_{rep} values, a given pair of comb modes will satisfy the resonance

condition for a unique velocity class. If the velocity distribution of the atoms contains the on-resonance velocity class, then those atoms will be excited by a stepwise doubly resonant transition. Thus, the relative size of the peaks depends on the number of the atoms in the velocity class.

4

Experiment

4.1 Setup

The experimental setup is shown in Figure 4.1. The polarization of the comb light is first rotated by a half-wave plate at 800 nm. The light is then frequency-broadened with the microstructure fiber so that is spans an optical octave for the purpose of f_0 stabilization. In some spectrum measurements, to control for polarization, we placed a polarizing cube after the microstructure fiber. The light is then filtered by an interference filter to contain the 795 nm, 780 nm, and 776 nm light needed to make the two-photon transition to the 5D states, shown in Figure 3.1 in the previous chapter. We used one of four different filters: three filters centered around 770 nm, 785 nm, 780 nm with 20 nm passbands, and a broader frequency range red filter centered around 810 nm. Their transmittance spectra are shown in Figure 4.2.

The near-infrared light from the interference filter was then focused down by a 10 cm lens and aligned to go through a 15 cm lens, then through a hole in the side of a light-proof box and through the side of a rubidium vapor cell. The light was then reflected by another mirror to go back through another 15 cm lens and through the vapor cell, and the laser was aligned such that the incoming beam and the reflected beam were counterpropagating, thus canceling out the Doppler broadening mentioned in section 3.5.2.

The vapor cell was wrapped in ~ 8 m of insulated steel wire, which was secured by Teflon tape. The wire had a resistance of 180 Ω and was used to heat the vapor cell to about 320 K, which was measured by securing a thermocouple to the cell. To decrease

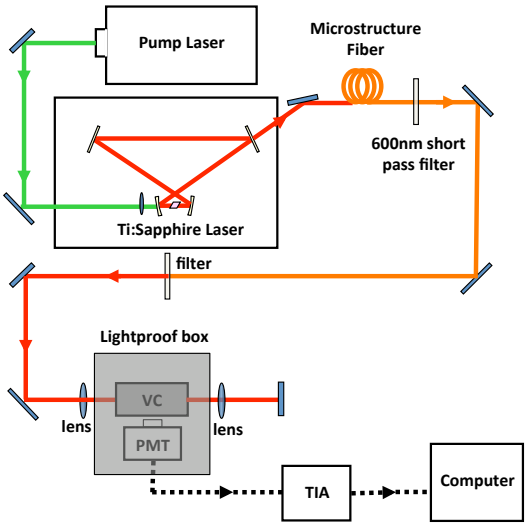

Figure 4.1: The setup for the experiment. The output of the comb is filtered for the 776 nm, 780 nm, and 796 nm light for the various two-photon transitions. This light is focused down by a lens and directed into a pinhole in the side of a lightproof box through the vapor cell. If the atoms undergo a two-photon transition, the fluorescence is detected by a photomultiplier tube (PMT). The current from the PMT is converted into a voltage by the transimpedance amplifier (TIA), which is then interfaced with a computer.

thermal conductivity, the vapor cell was wrapped in a layer of insulation. At 320 K, the vapor density was on the order of 10^{11} atoms/cm^3, as shown in Figure 4.3.

To measure the spectrum, the frequency-stabilized comb scanned through different values of f_{rep} in the method explained in section 2.4. A Hamamatsu H6780 photomultiplier tube (PMT) was used to detect fluorescence from the atoms. A PMT detects photons via the photoelectric effect; incoming photons eject electrons off the cathode of the PMT, and these electrons are accelerated through a series of electrodes to create an amplified current. This particular PMT model has an effective diameter of 8 mm, a typical gain of 1×10^6 and a dark current of 2 nA. Dark current is a source of noise that is inherent to all light-sensitive devices.

The current from the PMT is then turned into a voltage and amplified by a transimpedance amplifier (TIA). The TIA is essentially an integrating circuit with a zero impedance input, pictured in Figure 4.4; it averages an input current over a period of time. Our TIA was set to a gain of 10^7 V/A.

A 420 nm interference filter with a 20 nm passband was attached to the PMT, which means that it could only detect the 422 nm fluorescence that results from the

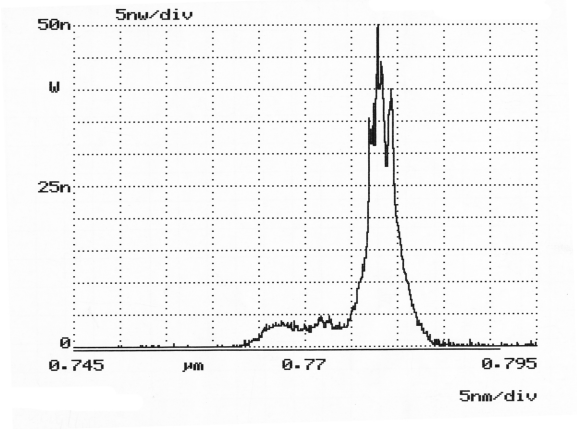

(a) 770 nm filter transmission spectrum

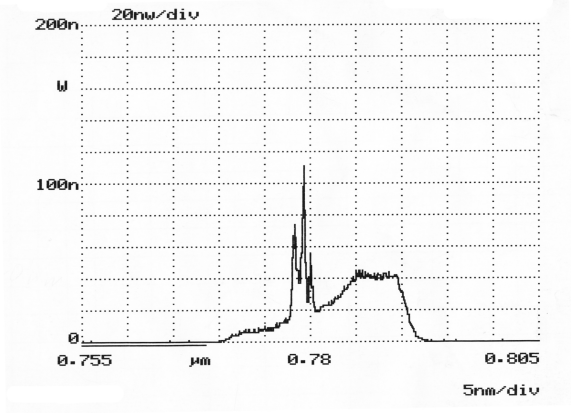

(b) 780 nm filter transmission spectrum

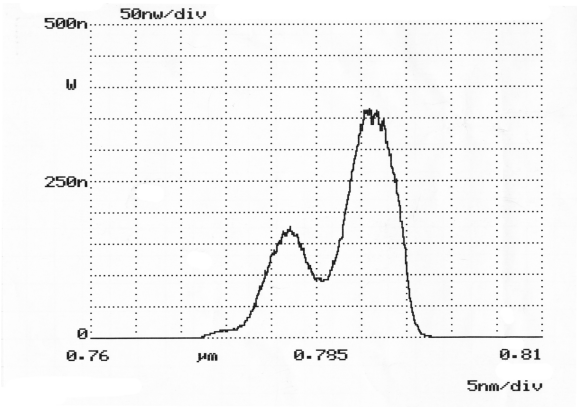

(c) 785 nm filter transmission spectrum

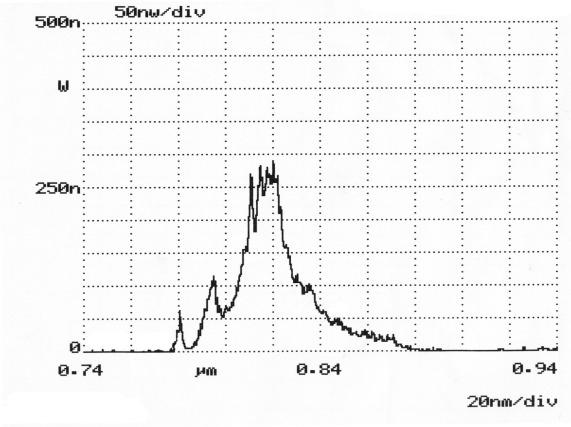

(d) Broad range red filter transmission spectrum

Figure 4.2: The transmission spectra of interference filters used in this experiment.

two-photon transition decay from the $5D$ states through the $6P$ states, as mentioned in section 3.2. When one of the comb modes was on-resonance with the two-photon transition for a certain velocity class of the atoms, the PMT detected the fluorescence from their decay.

The synthesizer to which the f_{rep} lock was referenced scanned through a range of f_{rep} from 924.730200-924.731730 MHz in 1 Hz steps, while f_0 was locked to 250 MHz.

Once this fluorescence was converted to a voltage by the TIA, this signal was interfaced with a Labview program on a computer. The program recorded measurements from the TIA 20000 times per second. It then averaged 2000 of the measurements together for an averaging time of 0.1 s, and its output was a data file of these averaged

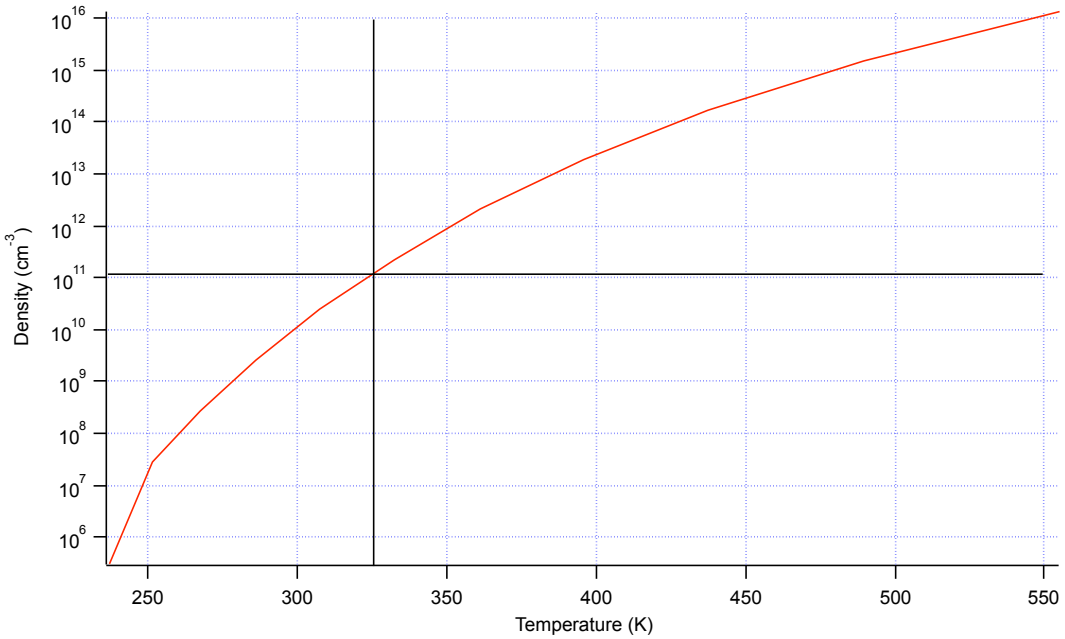

Figure 4.3: The vapor cell was heated to about 320K, such that the vapor density was on the order of 10^{11} atoms per cubic centimeter. Values taken from Ref. [24].

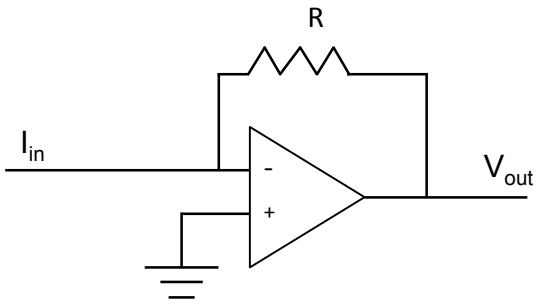

Figure 4.4: A transimpedance amplifier converts a current into an voltage by essentially behaving like an operational amplifier with zero input impedance. The golden rules for op amps state that the inputs (+ and -) draw no current, and the inputs are at the same voltage. Thus, $V_{out} = I_{in}R$.

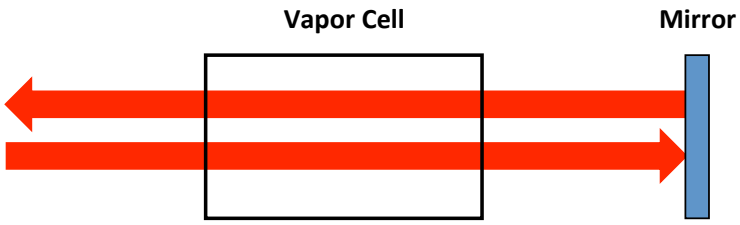

Figure 4.5: The beam is reflected back through the vapor cell using a mirror. The beam is aligned to reflect back on itself but is shown unaligned here for clarity. This results in three possible resonance conditions: 1) where the atom is excited to both transitions by only the incoming beam, 2) only the reflected beam, or 3) it is excited to the first transition by the incoming beam and to the second transition by the reflected beam.

measurements. In other words, each point in the spectrum corresponded to a 1 Hz step in f_{rep}, and each point was averaged over 0.1 s.

In addition, using an 8% reflective beamsplitter, a fraction of the laser light from the comb was aligned into a photodiode. The LabView program also recorded the output voltage of this photodiode, which is proportional to the intensity of the beam. The fluctuations in the intensity of the mode led to a systematic error in each data point. We used the recorded photodiode voltage to eliminate this systematic error. This process is explained in more detail in Section 5.2.

The LabView program also recorded the voltage that controlled the AOM used in f_0 stabilization. This was used during data analysis to discard the noisy data where the f_0 lock was not stabilized.

4.2 Resonance from Counterpropagating and Copropagating Beams

The beam from the laser is set up as in Figure 4.5, where the incoming beam is then reflected back along itself. Because the ground-to-intermediate resonance is so close in energy to the intermediate-to-final resonance, this setup creates three possible conditions for a two-photon resonance: 1) an atom could be excited to both transitions with only the incoming beam, 2) only the reflected beam, or 3) it could be excited to the first transition by the incoming beam and excited to the second transition by the reflected beam.

The first two resonance conditions, where the both resonance conditions occur due to a copropagating beam, are a noteworthy characteristic of rubidium. These conditions arise from the two transitions in rubidium being so close in frequency such that the interference filter will allow both frequencies through. The predicted result of these beams result in a Doppler-broadened background.

The third resonance condition, where the two-photon transition arises from counter-propagating beams, is the only condition where velocity selective resonance is satisfied, which is discussed in section 3.7. The counterpropagation of the two beams excites a single velocity class of the atoms, canceling out the Doppler broadening of the peak.

4.3 Controlling Systematic Uncertainty

We accounted for several sources of systematic uncertainty in this experiment, including external magnetic fields, the intensity of the modes used in the two-photon transitions, and the polarization of the comb output light.

To cancel external magnetic fields at the rubidium vapor cell, three sets of Helmholtz coils were constructed and arranged around the vapor cell. The intensity of the modes were measured on a photodiode throughout the scan, whose output voltage was calibrated to an intensity. For some scans, the polarization of the comb light was controlled by placing a polarizing cube after the microstructure fiber.

5

Results

In this section, we compare our experimentally measured spectra with our spectra calculations, and we discuss some of the uncertainties in the experiment. Because we have not extracted precise measurements from the measured spectra, we do not go through a rigorous error analysis.

5.1 Spectra Calculations

In order to better understand our experimental data, we ran models that simulated the experimental setup of the comb exciting a sample of rubidium. The model included only a few modes of the comb to expedite the computation. The model produced calculated spectra by simulating the comb scanning through a range of f_{rep} values for a fixed f_0 value.

The models accounted for all of the theoretical characteristics mentioned in the theory section. The energies for the D_1 and D_2 transitions were found in Refs. [3, 4]. The hyperfine energies for the ground state to $5D_{\frac{3}{2}}$ and $5D_{\frac{5}{2}}$ were found in Ref. [5]. The relative heights of the peaks were calculated using the $6j$ and $3j$ symbols, and the probability calculation included two of the three resonance conditions mentioned in Section 4.2, the resonance from counterpropagation and one of the copropagation resonances. The other copropagation resonance was excluded to make the program faster, as the copropagation terms did not contribute much compared to the counter-propagation term.

An example of a spectrum calculation notebook is included in the appendix.

5.2 Data Averaging

The raw output of the LabView program was many data files over the same f_{rep} range. To reduce statistical uncertainty, these files were averaged together using Igor Pro and Mathematica scripts.

The Igor Pro script power-normalized each of the data files in the following way. A fraction of the laser light had been aligned into a photodiode. First, a background intensity was measured by blocking all laser light. This background voltage was subtracted from each data file. A photodiode picked off a fraction of the laser light, and fluctuations in the intensity of this light were proportional to the fluctuations in the intensity of the light used to excite the rubidium. Because transition probability is proportional to the intensity squared, we divided each point in the data file with its corresponding measured intensity squared. This eliminated the power dependence of each data point.

Then, these power-normalized data files were averaged using a Mathematica script. The Mathematica script first discarded all the points where the f_0 was not stabilized, and then combined all the scans that used the same interference filters over the same f_{rep} range and averaged them together.

5.3 Peak Identification and Analysis

The peaks were first roughly identified by running a spectra calculation mentioned in Section **??** with the most recent literature values for our transitions of interest. We first determined whether the f_0 was positive or negative. The ambiguity in the sign of f_0 arises because we lock f_0 to a beat frequency equal to $|2\nu_n - \nu_{2n}|$. Thus, we do not know if we are locked to $f_0 = 2\nu_n - \nu_{2n}$ or $f_0 = \nu_{2n} - 2\nu_n$, where ν_n is the frequency-doubled comb mode with mode number n, and ν_{2n} is the comb mode with mode number $2n$.

We determined that $f_0 = +250$ MHz by running calculations for both signs of f_0 and qualitatively comparing the calculated spectra to our experimentally measured spectra.

Qualitatively, the positions of the peaks of our calculated spectra match our experimentally measured peaks.

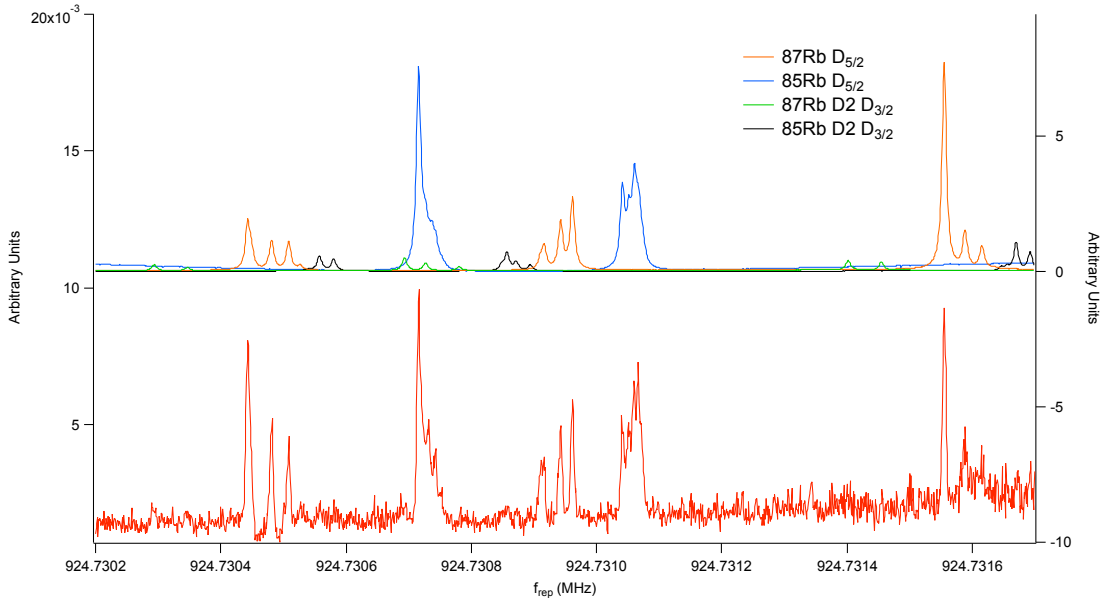

Figure 5.1: This plot shows a power-normalized, averaged spectrum on the left axis, measured with a 770 nm interference filter. The spectra calculations are on the right axis and are weighted by isotopic abundance. The transitions through intermediate transition D_1 are not visible because the transitions are at 795 nm and 762 nm, which are not passed well by this interference filter (see Figure 4.2 for transmittance spectra). The $D_{\frac{3}{2}}$ transitions are smaller than the $D_{\frac{5}{2}}$. The axes have arbitrary units proportional to transition probability.

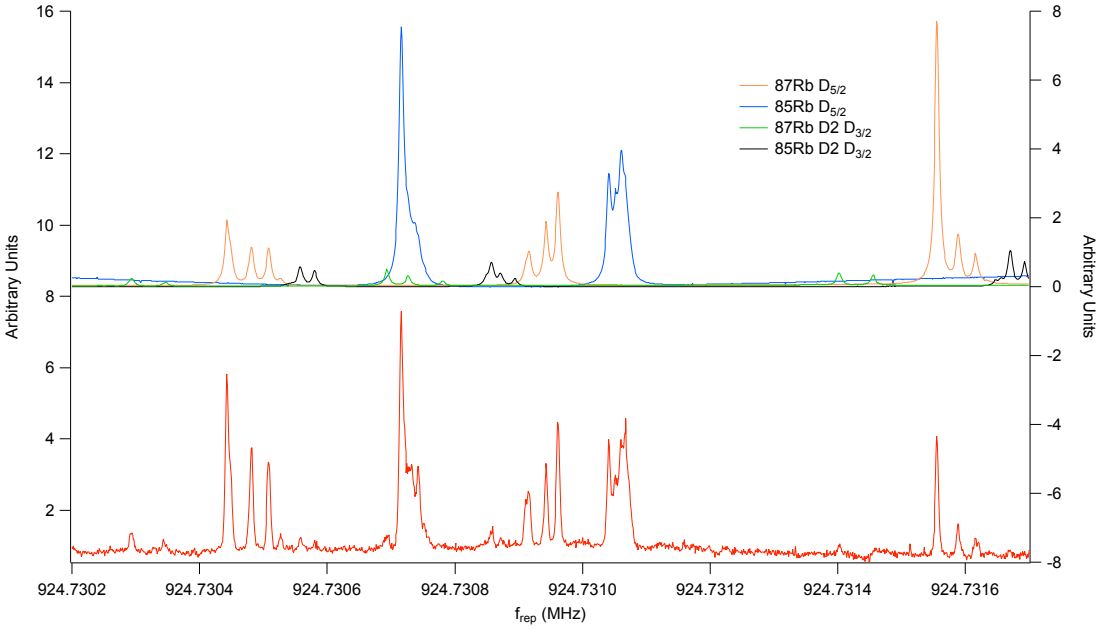

Figure 5.2: This plot shows a power-normalized, averaged spectrum on the left axis, measured with a 780 nm interference filter. The spectra calculations are on the right axis and are weighted by isotopic abundance. The transitions through intermediate transition D_1 are not visible because the transitions are at 795 nm and 762 nm, which are not passed well by this interference filter (see Figure 4.2 for transmittance spectra). The $D_{\frac{3}{2}}$ transitions are smaller than the $D_{\frac{5}{2}}$. The axes have arbitrary units proportional to transition probability.

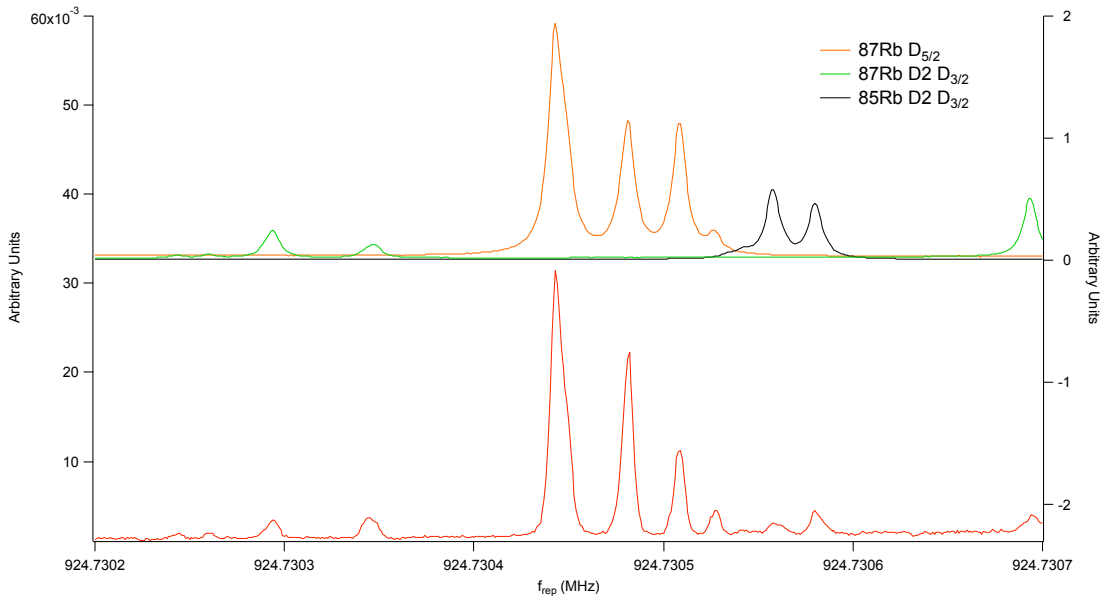

Figure 5.3: This plot shows a power-normalized, averaged spectrum on the left axis, measured with a 785 nm interference filter. The spectra calculations are on the right axis and are weighted by isotopic abundance. The D_1 transitions are not visible because the transitions are at 795 nm and 762 nm, which are not passed well by this interference filter (see Figure 4.2 for transmittance spectra). The $D_{\frac{3}{2}}$ transitions are smaller than the $D_{\frac{5}{2}}$. The axes have arbitrary units proportional to transition probability.

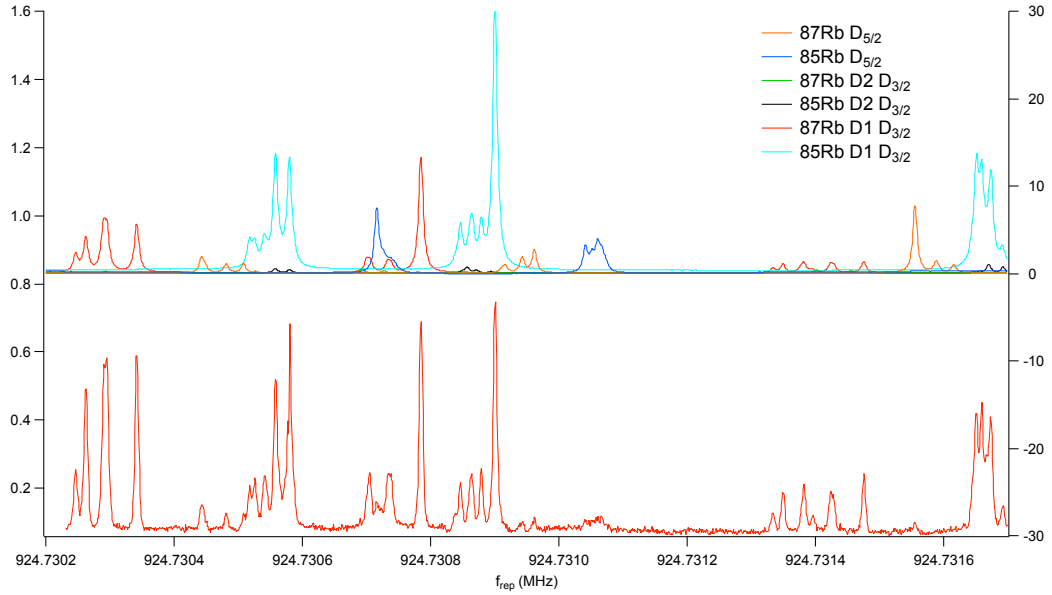

Figure 5.4: This plot shows a power-normalized, averaged spectrum on the left axis, measured with a broad range red interference filter. The spectra calculations are on the right axis and are weighted by isotopic abundance. Unlike the previous plots, the D_1 transitions are evident because of the larger transmittance range of this filter (see Figure 4.2 for transmittance spectra). However, the relative amplitudes predicted by the calculation do not agree with the experimental spectrum; for example, compare the yellow calculated spectrum, from the $D_{\frac{5}{2}}$ transition in ^{87}Rb, to the measured spectrum. The axes have arbitrary units proportional to transition probability.

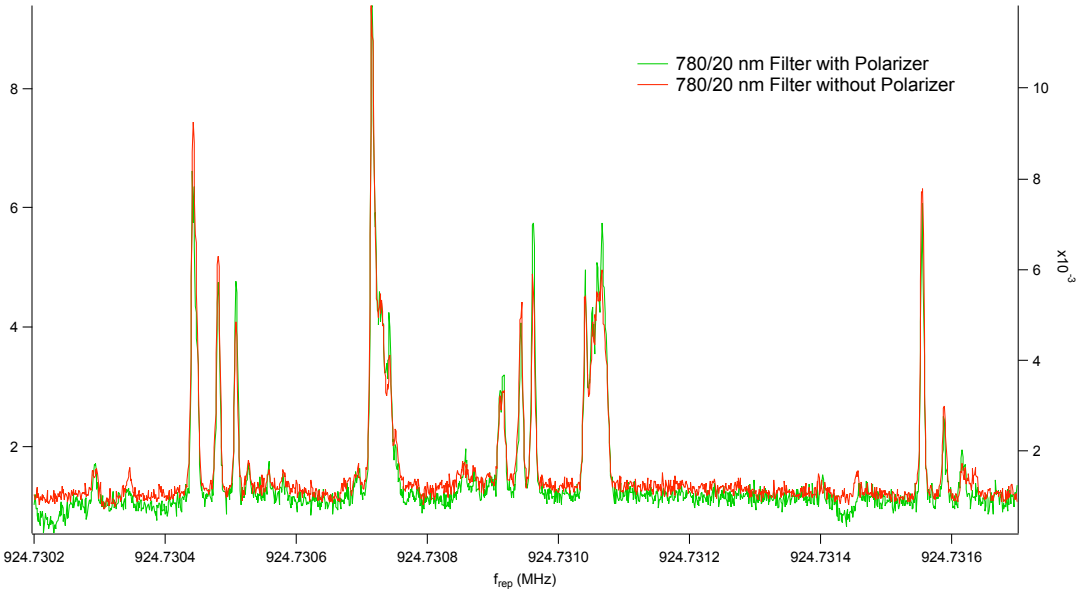

Figure 5.5: This plot shows two power-normalized spectra taken with the 780 nm interference filter. The scans are overlaid on top each other. The green spectrum was taken with a polarizing cube placed after the fiber to control for polarization, while the red spectrum had no polarizing cube. Qualitatively, the relative amplitudes of the peaks do not change much. This indicates that without the polarizing cube, the polarization of the light from the comb is already close to linearly polarized. The axes have arbitrary units proportional to transition probability.

As indicated in Figure 5.5, the addition of the polarizing cube did not change relative amplitudes, which indicates that the light from the comb was already mostly linearly polarized.

In addition, the Doppler broadened background predicted in spectra calculation is not present in the measured spectra. This may be because the intermediate resonance condition is not met by any large velocity class for the copropagating beams.

While the location of the peaks match up well to the spectra calculation in Figures**??**, the linewidths, taken from Refs. [14, 20] are not correct. This may be due to misalignment of the counterpropagating beams. If the counterpropagating beams are not exactly aligned, Doppler broadening is still present.

Finally, the relative amplitudes predicted by the spectra calculation are incorrect. We have not yet resolved the reason behind this discrepancy between calculation and experiment.

5.4 Sources of Uncertainty

The main sources of uncertainty in this experiment arise from pressure broadening, stray magnetic fields, and AC Stark shifts. Pressure broadening is explained in Section 3.5.3. Stray magnetic fields can lead to Zeeman splitting of energy levels, explained in Ref. [15]. AC Stark shifts are also known as light shifts and are explained in more detail in Ref. [16].

In the next sections, we explain why the uncertainty in the frequencies of the comb is negligible.

5.4.1 Frequency Standard Characterization

The frequency synthesizers in this experimental setup for stabilizing f_{rep} and f_0 used GPS-referenced rubidium atomic clocks as frequency standards.

An Allan deviation was calculated to test the frequency stability of the clock. A standard deviation calculation is not informative for measuring clock stability because clocks tend to diverge in the long-term, and thus the standard deviation over time also diverges. The Allan deviation avoids this divergence by using the deviation between adjacent points, rather than the deviation of the entire data set. Analogous to the

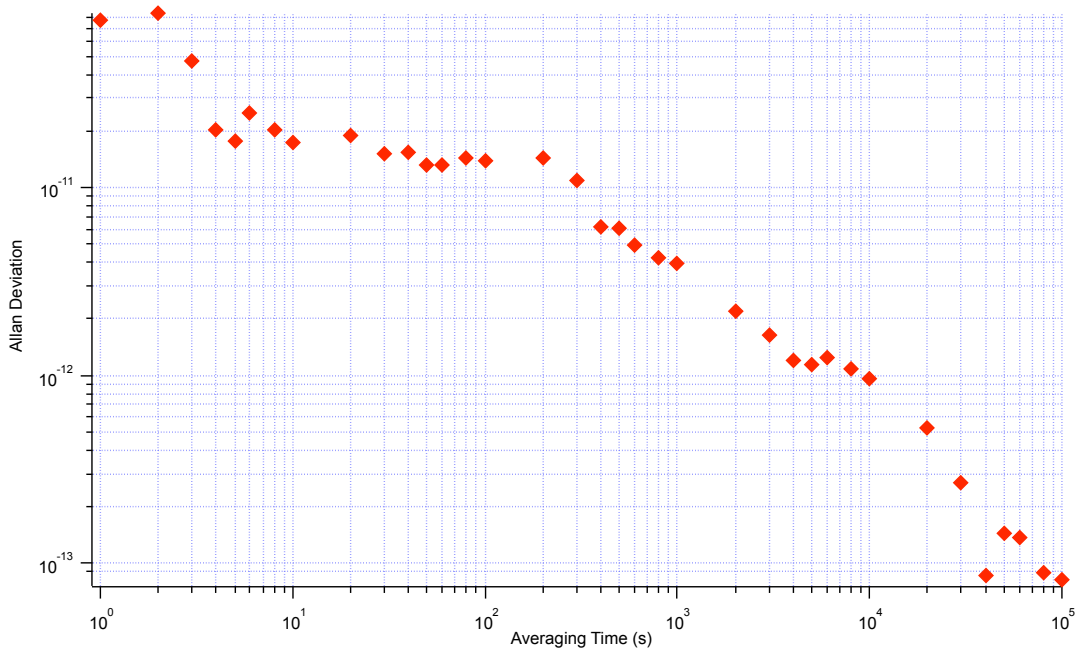

Figure 5.6: The Allan deviation of our frequency standard, a rubidium clock, averaged over a day. The plot indicates that the fractional uncertainty in our averaging time is about two in 10^{-11}. Thus, the stability of the clock is not the limiting factor of our uncertainty in this experiment.

relation between mean standard deviation and mean variance, the square of the Allan deviation is called the Allan variance.

The frequency standard is set to count a certain frequency for a period of time. In this experiment, these counts were recorded by a LabView program every second. The algorithm for the Allan deviation consists of the following: let the first three points in time be f_1, f_2, and f_3, respectively. The difference δf_1 is calculated between f_1 and f_2 and is a measurement of the deviation per second. This difference is then calculated for each pair of adjacent points, for a total of $(n-2)$ times, where n is the number of points. The Allan deviation σ_A, which is a sort of average of these $(n-2)$ deviations, is then calculated, and is defined as

$$\sigma_A = \sqrt{\frac{\sum_{i=1}^{n-2} (\delta f_i)^2}{2(n-2)}}. \tag{5.1}$$

In this case, σ_A is a measurement of clock stability for an averaging time of 1 second. This process is then repeated for averaging times of two seconds, three seconds, etc. For example, in the two-second averaging time case, the first two points are averaged together and subtracted from the average of the third and fourth points to get δf_1. These deviations are then plotted versus averaging time, as seen in Figure 5.6. The last point in the Allan deviation plot compares the average frequency of the first half of the points with the average frequency of the last half of the points. The last few points should have the lowest deviation, but it is important to note that they have a much greater uncertainty than the first few points because they are averaged over so few points [1].

Figure 5.6 indicates that the fractional uncertainty in our averaging time is about two in 10^{-11}. This uncertainty is below the uncertainty in our measurement, which means that the the uncertainty in the frequency standard is not the limiting factor in this experiment.

In addition, the uncertainty from the frequency stabilization in f_{rep} and f_0 are negligible, which means that the uncertainty from the frequency of the comb is negligible.

Figure 5.7 shows the Allan deviation of the f_{rep} lock overlaid on the stability of two GPS-referenced rubidium clocks, one referenced to the other. The black line is a $1/\sqrt{\tau}$ line, which represents the standard deviation of the noise if it followed a normal

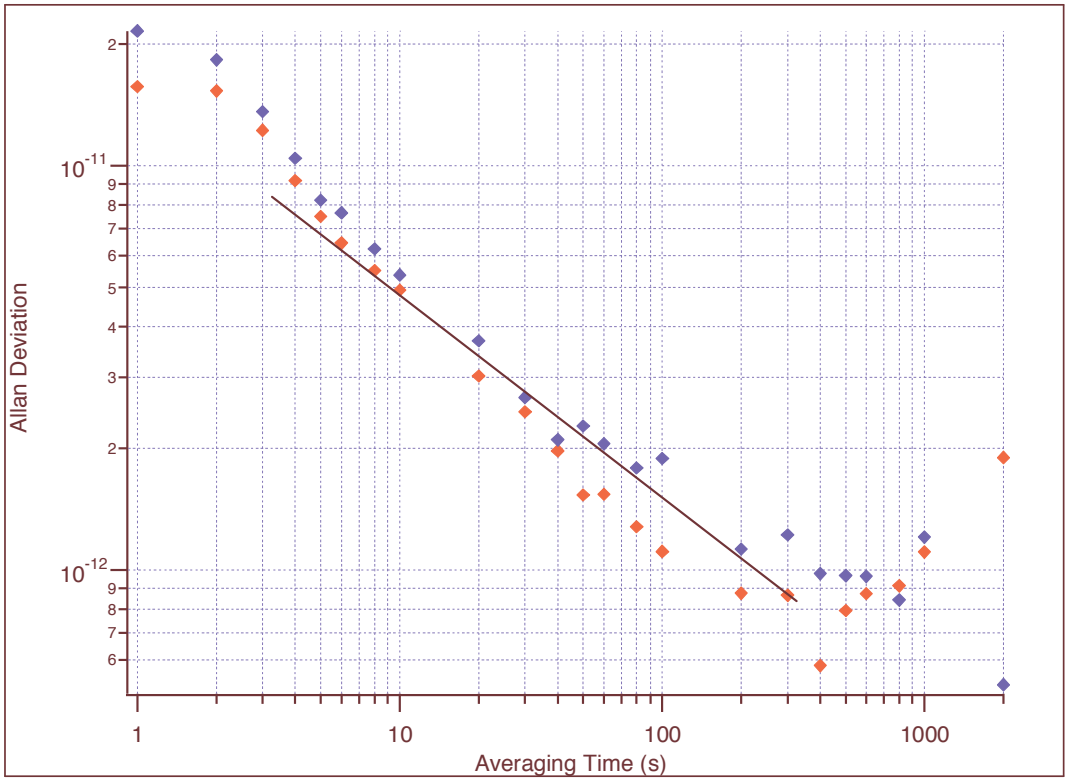

Figure 5.7: This plot shows the Allan deviation for the GPS-referenced rubidium clock in red, and the Allan deviation for the stability of the f_{rep} lock in blue. The black line is a $1/\sqrt{\tau}$ line, which is the Allan deviation for when only stochastic noise is present. Figure taken from Ref. [6].

distribution [6]. The fractional uncertainty of the f_{rep} lock is on the order of 10^{-11}, indicating that very little noise in the measurement is due to the stability of f_{rep}.

The f_0 lock also contributed negligible noise. Measured on a spectrum analyzer, the linewidth of the f_0 beat was less than 500 kHz, which is a fractional uncertainty on the order of $\sim 10^{-3}$. However, the uncertainty on f_0 was actually even smaller because while the linewidth was on the order of kHz, the center frequency to which f_0 is locked, was fluctuating on the order of mHz, which means that f_0 had a fractional uncertainty $\sim 10^{-9}$.

Thus, from these order of magnitude uncertainty estimations of the frequency locks and the atomic clock frequency standard, the uncertainty in the frequency stabilization of the comb were not the limiting factors in this experiment.

5.5 Conclusions and Future Work

The measured spectra is promising; the qualitative agreement in the positions of the peaks with our spectra calculation indicate that we are on the right track to understanding our system. The next step is to refine our spectra calculations so they agree better with the measurements. Namely, we need to figure out why the relative amplitudes in our calculated spectra do not agree with the experimental measurements, and we also need to establish the sources of the linewidth.

We are also working to understand DFCS better. Currently, we are comparing the rubidium spectra collected with our frequency comb, with an $f_{rep} \sim 1$ GHz, with the spectra taken with a comb with an $f_{rep} \sim 200$ MHz. This comparison may illuminate new aspects of the DFCS.

In addition, the success of this technique for spectroscopy indicates that DFCS could be applied to spectroscopy of less precisely-studied atoms or more complicated systems. One of the logical next steps is to study the spectrum of potassium, which we have already attempted. The adjustment of the experimental setup is simple; it requires the use of different interference filters and realignment. However, the transition probabilities of potassium are much lower than rubidium, making the experiment noisier and more difficult.

Appendix

Appendix A

Mathematica Spectra Calculations

The following is an example of a Mathematica spectrum calculation used in this thesis. The code calculates the spectrum of ^{87}Rb due to the transitions from ground state to $5D_{\frac{5}{2}}$ via the D_2 transition. Comments are written in both Mathematica comment syntax and in the unbolded font.

```
Off[ClebschGordan::"tri"];
Off[ClebschGordan::"phy"];
```

Speed of light in cm/sec

```
c = 29979245800; (*cm/sec*)
```

Planck's constant in ergs·sec

```
hBar = 1.054 10^-27; (*ergs sec*)
```

Boltzmann's constant in ergs/K

```
kB = 1.380658 10^-16; (*erg/K*)
```

Nuclear spin

$i = \frac{3}{2};$

Transit Linewidth

$\gamma T = \frac{1}{26.2\ 10^{-9}};$

Polarization

$q1 = \{0, 1, 0\};$

$q2 = \{0, 1, 0\};$

Ground State S

$SGnd = \frac{1}{2};$

Ground State J

$jGnd = \frac{1}{2};$

Ground State F Values

$fMinGnd = Abs[jGnd - i];$

$fMaxGnd = jGnd + i;$

Ground State Hyperfine A

$aGnd = SetPrecision[3417341305.452145, 20];$ (*From Steck*)

Ground State Hyperfine B

bGnd = 0;

Intermediate State S

SInt = $\frac{1}{2}$;

Intermediate State J

jInt = $\frac{3}{2}$;

Intermediate State F Values

fMinInt = Abs[jInt − i];

fMaxInt = jInt + i;

Intermediate State Linewidth, Ref. [20]

γInt = $\frac{1}{26.2\ 10^{-9}}$; (*SecondsFromBudker, Kimball, DeMille*)

Intermediate State Center of Gravity Frequency, Ref. [4]

νInt = SetPrecision[384230484468500, 20];

(*Hz from Steck*)

Intermediate State Hyperfine A

aInt = SetPrecision[84718500, 20]; (*Hz From Steck*)

Intermediate State Hyperfine B, Ref. [4]

bInt = SetPrecision[12496500, 20]; (*Hz From Steck*)

Final State S

SFin = $\frac{1}{2}$;

Final State J

jFin = $\frac{5}{2}$;

Final State F Values

fMinFin = Abs[jFin − i];

fMaxFin = jFin + i;

Final State Linewidth, Ref. [14]

γFin = $\frac{1}{241.\ 10^{-9}}$; (*Seconds From Heavens*)

Formula for Calculating Energies with Hyperfine Structure

κ[f_, j_] = $f(f+1) - j(j+1) - i(i+1)$;

δE[a_, b_, f_, j_]:=If $\left[j \neq \frac{1}{2} \&\& i \neq \frac{1}{2}, \frac{1}{2} a\kappa[f,j] + b\frac{\frac{3}{4}\kappa[f,j]^2 + \frac{3}{4}\kappa[f,j] - i(i+1)j(j+1)}{2i(2i-1)j(2j-1)}, \frac{1}{2} a\kappa[f,j]\right]$;

νGndToInt[f_, fPrime_] = νInt − δE[aGnd, bGnd, f, jGnd] + δE[aInt, bInt, fPrime, jInt];

νGndToFin[f_, fDPrime_]:=2Switch[{f, fDPrime},

{2, 4}, 385284566366300,

{2, 3}, 385284580777800,

{2, 2}, 385284592255200,

{2, 1}, 385284600225200,

{1, 3}, 385287998122200,

{1, 2}, 385288009600200,

{1, 1}, 385288017566900]

Reduced Matrix Elements in J Basis

dRedJGndToInt = 1;

(*(4.51)1.28 10^6(*Hz/(V/cm)*);*)

Reduced Matrix Elements in F Basis

```
Do[
Do[
dRedGndToInt_{f,fPrime} = √((2fPrime + 1)(2f + 1)SixJSymbol[{jInt, fPrime, i}, {f, jGnd, 1}]^2dRedJGn
{fPrime, fMinInt, fMaxInt}],
{f, fMinGnd, fMaxGnd}]
```

Matrix Elements in F Basis

```
Do[
Do[
dRedIntToFin_{fPrime,fDPrime} =
√((2fDPrime + 1)(2fPrime + 1)SixJSymbol[{jFin, fDPrime, i}, {fPrime, jInt, 1}]^2dRedJIntToFin^2),
{fDPrime, fMinFin, fMaxFin}], {fPrime, fMinInt, fMaxInt}]

Do[
Do[
Do[
Do[
dGndToInt_{f,fPrime,m,mPrime} =
(-1)^{fPrime-mPrime} ∑_{n=1}^{3} (q1[[n]]ThreeJSymbol[{fPrime, -mPrime}, {1, n - 2}, {f, m}])dRedGndToInt
{m, -f, f}],
{mPrime, -fPrime, fPrime}],
{fPrime, fMinInt, fMaxInt}],
{f, fMinGnd, fMaxGnd}];

Do[
Do[
Do[
```

```
Do[
dIntToFin_{fPrime,fDPrime,mPrime,mDPrime} =
(-1)^(fDPrime-mDPrime) Sum_{n=1}^{3} (q2[[n]] ThreeJSymbol[{fDPrime, -mDPrime}, {1, n - 2}, {fPrime, mPrime}])
dRedIntToFin_{fPrime,fDPrime},
{mPrime, -fPrime, fPrime}],
{mDPrime, -fDPrime, fDPrime}],
{fDPrime, fMinFin, fMaxFin}],
{fPrime, fMinInt, fMaxInt}];
```

Doppler Distribution Parameters

```
mRb = 1.41 10^-22;
temp = 323;

α = √(2kBtemp / mRb)

dopplerDist[v_]:=Exp[-v^2/α^2]
```

Comb Parameters

Offset Frequency

```
f0 = 250. 10^6;
```

f_{rep} range

```
fRepMin = 924.730200 10^6;
fRepMax = 924.731700 10^6;

fRepAvg = (fRepMin+fRepMax)/2;
```

Comb Modes

$$\text{n1NomA} = \text{Round}\left[\frac{\nu\text{GndToInt}[\text{fMinGnd},\text{fMinInt}]}{\text{fRepAvg}}\right];$$
$$\text{n1NomB} = \text{Round}\left[\frac{\nu\text{GndToInt}[\text{fMaxGnd},\text{fMaxInt}]}{\text{fRepAvg}}\right];$$

$$\text{n2NomA} = \text{Round}\left[\frac{1}{\text{fRepAvg}}(\nu\text{GndToFin}[\text{fMinGnd},\text{fMinFin}] - \nu\text{GndToInt}[\text{fMinGnd},\text{fMinInt}])\right];$$
$$\text{n2NomB} = \text{Round}\left[\frac{1}{\text{fRepAvg}}(\nu\text{GndToFin}[\text{fMaxGnd},\text{fMaxFin}] - \nu\text{GndToInt}[\text{fMaxGnd},\text{fMaxInt}])\right];$$

$$\text{n1List} = \text{Union}[\text{Join}[\text{Table}[\text{n1NomA} + \delta\text{n}, \{\delta\text{n}, -3, 3\}], \text{Table}[\text{n1NomB} + \delta\text{n}, \{\delta\text{n}, -3, 3\}]]]$$

$$\{415500, 415501, 415502, 415503, 415504, 415505, 415506, 415507, 415508, 415509, 415510, 415511, 4155$$

$$\text{n2List} = \text{Union}[\text{Join}[\text{Table}[\text{n2NomA} + \delta\text{n}, \{\delta\text{n}, -3, 3\}], \text{Table}[\text{n2NomB} + \delta\text{n}, \{\delta\text{n}, -3, 3\}]]]$$

$$\{417784, 417785, 417786, 417787, 417788, 417789, 417790, 417791\}$$

Comb Equation

$$\omega\text{L}[\text{n\_}, \text{fR\_}] := 2\pi(n\text{fR} + \text{f0});$$

Integrate 2-photon lineshape over Doppler Distribution

$$\text{transProb}[\omega 1\_, \omega 2\_, \text{v\_}] =$$
$$\sum_{\text{fDPrime}=\text{fMinFin}}^{\text{fMaxFin}} \sum_{f=\text{fMinGnd}}^{\text{fMaxGnd}} \left(\left(\frac{(\gamma\text{Fin}+\gamma\text{T})^2}{4} / \left((2\pi\nu\text{GndToFin}[f,\text{fDPrime}] - \omega 1\left(1+\frac{v}{c}\right) - \omega 2\left(1-\frac{v}{c}\right)\right)^2\right.\right.$$
$$\left.\left.\frac{(\gamma\text{Fin}+\gamma\text{T})^2}{4} / \left((2\pi\nu\text{GndToFin}[f,\text{fDPrime}] - \omega 1\left(1+\frac{v}{c}\right) - \omega 2\left(1+\frac{v}{c}\right)\right)^2 + \frac{(\gamma\text{Fin}+\gamma\text{T})^2}{4}\right)\right)$$
$$\frac{1}{2f+1}\sum_{m=-f}^{f}\sum_{\text{mDPrime}=-\text{fDPrime}}^{\text{fDPrime}} \text{Abs}\left[\sum_{\text{fPrime}=\text{fMinInt}}^{\text{fMaxInt}}\sum_{\text{mPrime}=-\text{fPrime}}^{\text{fPrime}}\right.$$
$$\left.\left(\frac{\gamma\text{Int}+\gamma\text{T}}{2} / \left(\frac{i(\gamma\text{Int}+\gamma\text{T})}{2} + \left(\omega 1\left(1+\frac{v}{c}\right) - 2\pi\nu\text{GndToInt}[f,\text{fPrime}]\right)\right)\right)\right.$$
$$\left.\text{dGndToInt}_{f,\text{fPrime},m,\text{mPrime}}\text{dIntToFin}_{\text{fPrime},\text{fDPrime},\text{mPrime},\text{mDPrime}}\right]^2 +$$
$$\left(\frac{(\gamma\text{Fin}+\gamma\text{T})^2}{4} / \left((2\pi\nu\text{GndToFin}[f,\text{fDPrime}] - \omega 1\left(1-\frac{v}{c}\right) - \omega 2\left(1-\frac{v}{c}\right)\right)^2 + \frac{(\gamma\text{Fin}+\gamma\text{T})^2}{4}\right) +$$
$$\frac{(\gamma\text{Fin}+\gamma\text{T})^2}{4} / \left((2\pi\nu\text{GndToFin}[f,\text{fDPrime}] - \omega 1\left(1-\frac{v}{c}\right) - \omega 2\left(1+\frac{v}{c}\right)\right)^2 + \frac{(\gamma\text{Fin}+\gamma\text{T})^2}{4}\right)\right)$$
$$\frac{1}{2f+1}\sum_{m=-f}^{f}\sum_{\text{mDPrime}=-\text{fDPrime}}^{\text{fDPrime}} \text{Abs}\left[\sum_{\text{fPrime}=\text{fMinInt}}^{\text{fMaxInt}}\sum_{\text{mPrime}=-\text{fPrime}}^{\text{fPrime}}\right.$$
$$\left.\left(\frac{\gamma\text{Int}+\gamma\text{T}}{2} / \left(\frac{i(\gamma\text{Int}+\gamma\text{T})}{2} + \left(\omega 1\left(1-\frac{v}{c}\right) - 2\pi\nu\text{GndToInt}[f,\text{fPrime}]\right)\right)\right)\right.$$

$$\text{dGndToInt}_{f,\text{fPrime},m,\text{mPrime}}\,\text{dIntToFin}_{\text{fPrime},\text{fDPrime},\text{mPrime},\text{mDPrime}}\,]^{2})\,;$$

$$\text{fnToIntegrate}[\text{fR\_},\text{v\_}] = \sum_{\text{n1}=1}^{\text{Length[n1List]}} \sum_{\text{n2}=1}^{\text{Length[n2List]}} \text{dopplerDist}[v]\,\text{transProb}[\omega\text{L}[\text{n1List}[[\text{n1}]],\text{fR}],\omega\text{L}[\text{n2List}[[\text{n2}]],\text{fR}],v];$$

$$\text{vIntSpec}[\text{fRep\_?NumericQ}]:=\text{NIntegrate}[\text{fnToIntegrate}[\text{fRep},v],\{v,-60000,60000\},\text{MinRecursion}\to 3,$$
$$\text{MaxRecursion}\to 10,\text{AccuracyGoal}\to 4,\text{PrecisionGoal}\to 2];$$

Calculation

$$\delta\text{f} = 1;$$

```
Timing[
{
fRepList = {};
specList = {};
fRep = fRepMin;
n = 0;
While[fRep < fRepMax,
{
n+=1;
fRepList = Append[fRepList, fRep];
specList = Append[specList, Chop[vIntSpec[fRep]]];
totalSpec = Table[{fRepList[[t]], specList[[t]]}, {t, 1, Length[specList]}];

fRep+=δf;
}];
```

```
Print[specFile];

}]

Export["C:\\Jason\\MathematicaStuff\\RbCalcs\\120224\\87Rb52D2\\Rb87D52D2.txt", totalSpec

ListPlot[totalSpec, PlotRange → All, Joined → False]
```

References

[1] David W. Allan, Neil Ashby, and Clifford C. Hodge. *The Science of Timekeeping: Application Note 1289*. Hewlitt-Packard.

[2] Theodor W. Hänsch. **Nobel Lecture: Passion for precision**. *Reviews of Modern Physics*, **78**, 2006.

[3] Daniel Adam Steck. *Rubidium 85 D Line Data*. Oregon Center for Optics and Department of Physics, 0.1.1 edition, 2008.

[4] Daniel Adam Steck. *Rubidium 87 D Line Data*. Oregon Center for Optics and Department of Physics, University of Oregon, 2.0.1 edition, 2001.

[5] F. Nez, F. Biraben, R. Felder, and Y. Millerioux. **Optical frequency determination of the hyperfine components of the $5S_{1/2}$-$5D_{3/2}$ two-photon transitions in rubidium**. *Optics Communications*, 1993.

[6] Sean Bernfeld. *Stabilization of a Femtosecond Frequency Comb*. Honors thesis, Oberlin College, 2009.

[7] Albrecht Bartels. **Chapter 3: Gigahertz Femtosecond Lasers: the tools for precise optical frequency metrology**. *Femtosecond optical frequency comb: principle, operation, and applications*, 2005.

[8] Anthony E. Siegman. *Lasers*. University Science Books, 1986.

[9] Jean-Claude Diels and Wolfgang Rudolph. *Ultrashort Laser Pulse Phenomena*. Academic Press, second edition, 2006.

[10] Matthew C. Stowe, Michael J. Thorpe, Avi Pe'er, Jun Ye, Jason E. Stalnaker, Vladislav Gerginov, and Scott A. Diddams. **Direct Frequency Comb Specroscopy**. *Advances in Atomic, Molecular and Optical Physics*, **55**, 2008.

[11] B.H. Bransden and C.J. Joachain. *Physics of Atoms and Molecules*. New York: Longman Group, 1983.

REFERENCES

[12] D. Budker, W. Gawlik, D.F. Kimball, S.M. Rochester, V.V. Yashchuk, and A. Weis. **Resonant nonlinear magneto-optical effects in atoms**. *Reviews of Modern Physics*, **74**, October 2002.

[13] J.E. Sansonetti. **Wavelengths, Transition Probabilities, and Energy Levels for the Spectra of Rubidium (Rb I through Rb XXXVII)**. *J. Phys. Chem. Ref. Data*, **35**(1), 2006.

[14] O.S. Heavens. **Radiative Transition Probabilities of the Lower Excited States of the Alkali Metals**. *Journal of the Optical Society of America*, **51**(10), October 1961.

[15] David J. Griffiths. *Introduction to Quantum Mechanics*. Upper Saddle River, NJ: Pearson Prentice Hall, second edition, 2005.

[16] Alan Corney. *Atomic and Laser Spectroscopy*. Oxford University Press, 1977.

[17] Igor I. Sobelman. *Atomic Spectra and Radiative Transitions*. New York: Springer-Verlag, second edition, 1996.

[18] Claude Cohen-Tannoudji, Bernard Diu, and Franck Laloë. *Quantum Mechanics*, **2**. Wiley, 1977.

[19] W. Demtröder. *Laser Spectroscopy: Basic Concepts and Instrumentation*. Springer-Verlag, 1981.

[20] Dmitry Budker, Derek F. Kimball, and David P. DeMille. *Atomic Physics: An Exploration Through Problems and Solutions*. Oxford University Press, 2004.

[21] Harold J. Metcalf and Peter van der Straten. *Laser Cooling and Trapping*. Springer, 1999.

[22] Jason E. Stalnaker, Vela Mbele, Vladislav Gerginov, Tara M. Fortier, Scott A. Diddams, Leo Hollberg, and Carol E. Tanner. **Femtosecond frequency comb measurement of absolute frequencies and hyperfine coupling constants in cesium vapor**. *Physical Review A*, 2010.

[23] J.J. Sakurai. *Modern Quantum Mechanics*. Addison Wesley, 1994.

[24] I.K. Kikoin, editor. *Tablitsi Fizicheskikh Velichin (Tables of Physical Values)*. Atomizda, 1976.